This is a preprint, the final version is subject to change, of the American Mineralogist (MSA)
Cite as Authors (Year) Title. American Mineralogist, in press.
DOI: https://doi.org/10.2138/am-2018-6402

revision 1

Archaean hydrothermal fluid modified zircons at Sunrise Dam and Kanowna Belle gold deposits, Western Australia: Implications for post-magmatic fluid activity and ore genesis

Rui Wang[a*], Heejin Jeon[b], Noreen J. Evans[c]

[a]State Key Laboratory of Geological Processes and Mineral Resources, and School of Scientific Research, China University of Geosciences, Beijing 100083, China

[b]Department of Geosciences, Swedish Museum of Natural History, Box 50 007, SE-10405 Stockholm, Sweden

[c]School of Earth and Planetary Sciences, John de Laeter Centre, TIGeR, Curtin University, Perth, WA 6102, Australia

*Corresponding author.

Email: rw@cugb.edu.cn (Rui Wang)

Professor, School of Scientific Research, China University of Geosciences, Beijing 100083, China

ABSTRACT

In order to further our knowledge of ore genesis in one of Australia's preeminent ore districts, we have completed a comprehensive geochemical study of ore-related porphyritic intrusions from the Archaean Kanowna Belle and Sunrise Dam gold deposits (both > 10 Moz), Eastern Goldfields, Western Australia. Zircons (including samples from the newly developed Velvet mine) with ages ranging from 2.8 to 2.2 Ga, were investigated for O-OH isotopic signatures, trace element abundance, and U-Th-Pb compositions in order to elucidate the nature of the magmatic source and ore-related fluid. These intrusions have similarly high Sr/Y and La/Yb ratios to adakites from the Aleutian and Cook Islands, but lower $Mg^{\#}$ values and higher K_2O contents, suggesting they were derived from partial melts in a thickened crust. The modern analogues are postcollisional, high-Sr/Y granitoid porphyries in southern Tibet. Magmatic zircons have intermediate $\delta^{18}O$ values (+5‰ to +6.3‰), and estimated magmatic crystallization temperatures (Ti-in-zircon) in between 660–760°C. They are interpreted as having crystallized from positive $\delta^{18}O$ magmas during water-fluxed melting of juvenile lower crust. Hydrothermal fluid modified zircons are texturally indistinguishable from magmatic zircons, but their trace element, OH, and isotopic compositions are distinct. The involvement of hydrothermal fluid in zircon growth is evidenced by a negative correlation between OH content and $\delta^{18}O$. In addition, the studied hydrothermal fluid modified zircons are characterized by high La contents, flat rare earth element patterns, weak Ce anomalies, and high Eu/Eu* ratios, suggesting they were related to a high-temperature, Zr-saturated, high-Eu, Cl-rich, and low-pH hydrothermal fluid. Such fluids are common in eastern Yilgarn gold camps.

Keywords: hydrothermal fluid modified zircon, fluid, OH, O isotope, gold mineralization, Archaean

INTRODUCTION

The Eastern Yilgarn Craton is one of the largest gold camps in the world, with many giant gold deposits (e.g., Blewett et al., 2010; Goldfarb and Groves, 2015; Wang et al., 2017). In order to improve our understanding of gold genesis in the Eastern Yilgarn Craton, more precise geochronological and isotopic data are needed. Zircon is generally resistant to post-crystallization alteration, so the timing of gold mineralization can be either directly determined on hydrothermal zircon or indirectly constrained using magmatic zircon (Claoué-Long et al., 1988; Pelleter et al., 2007; Zhou et al., 2012). Zircon O-Hf isotopic signatures are widely used to indicate magmatic source composition. However, the effect of fluids on the U-Th-Pb and O isotope systems in pre-Proterozoic zircons has only been sparsely studied (Pidgeon et al. 2013). Pidgeon et al. (2017) proposed that low temperature fluids affected both the U-Th-Pb ages and O-OH isotopic compositions of zircons from Jack Hills. However, the effect of higher temperature ore fluids or post-magmatic fluids on Archaean zircons has not been welly investigated.

Two Archaean gold deposits (Sunrise Dam and Kanowna Belle), that formed at sub-amphibolite metamorphic facies conditions (~greenschist) in the Eastern Goldfields of Western Australia, show close association with Archaean felsic intrusions (Wang et al., 2017) and were subjected to a significant number of hydrothermal events. Zircons from these deposits were selected for detailed elemental and isotopic study in order to better understand the nature of post-magmatic fluids and their effect on zircon growth. This approach has enormous potential for determining fluid source and constraining the timing of mineralization.

GEOLOGICAL SETTING OF THE EAST YILGARN CRATON (EYC)

The Yilgarn craton is composed of six tectonostratigraphic terranes (Narryer, South West Gneiss, Youanmi, Kalgoorlie, Kurnalpi, and Burtville; Cassidy et al., 2006). The last three of these terranes constitute the EYC or Eastern Goldfields superterrane (Fig. 1), which is bounded by interconnected, NNE-striking and E-dipping crust-penetrating structures (Ida, Ockerburry, and Hootanui faults; Swager et al., 1995; Swager, 1997; Goleby et al., 2002, 2003; Cassidy et al., 2006; Blewett et al., 2010) that intersect the Moho. The deformation history of the EYC comprised six events identified as D1 (or DE), D2, D3, D4, D5, and D6 (Blewett et al., 2010).

The EYC is a major producer of Au, Ni, and Ta, as well as Al, Fe, Cu, W, Mo, Sn, Li, V, U, rare earth elements (REE) and Zr, and hosts many world-class gold and nickel deposits at Kalgoorlie and Kambalda, respectively. The gold mineralization is typically related to faults and shear zones that were initially established during D2 (~2670 Ma), but were then reactivated and became the focus for mineralizing fluid movement during D4 (~2625 Ma). Peak metamorphism during D2 to D6 was typically greenschist, although grades of amphibolite and even granulite facies were locally developed (Bateman and Bierlein, 2007; Vielreicher et al., 2010). Porphyries, albitites and lamprophyres are commonly found in the gold deposits, with the porphyries being broadly synchronous with Au (Vielreicher et al., 2015 and references therein). Traditionally, these deposits have been described as orogenic in style (e.g. Groves, 2003; Witt and Vanderhor, 1998; Goldfarb et al., 2015), however, some gold deposits with strong affinities to neighboring felsic intrusions could, in theory, be classified as skarn-, porphyry-, or epithermal-gold types (e.g. Mueller et al., 2008). Sulphur isotope signatures vary widely (-10 ‰ to +12.6 ‰ $\delta^{34}S$), indicating multiple mechanisms of gold precipitation in a range of structural settings (Hodkiewicz et al., 2009 and references therein).

DEPOSIT GEOLOGY

Sunrise Dam

The Sunrise Dam deposit is located at the eastern margin of the Kurnalpi Terrane (Fig. 1). The basal stratigraphy of the Kurnaipi terrane is mainly composed of mafic volcanic rocks, intermediate calc-alkaline complexes, and feldspathic sedimentary rocks. The overlying stratigraphy is bimodal, high-field-strength-element (HFSE) enriched rhyolite-basalt and intermediate-felsic calc-alkaline complexes (Cassidy, 2006). The Laverton domain includes mafic and ultramafic volcanic rocks, banded iron formation (BIF) and fine-grained tuffaceous sediments at the base. The Nd T_{DM2} ages (2.95–2.72 Ga) are younger than those from the Kalgoorlie terrane (Champion and Cassidy, 2007) and the Sunrise Dam deposit is mainly hosted within greenschist-facies basalts, doleritic sills, BIF, and volcanic sediments. A protracted deformation history with structural reactivation resulted in multiple phases of gold mineralization. There are several inter-connected orebodies within Sunrise Dam, including Astro, Cosmo, GQ, and Vogue and the intrusions selected for this study are located within the Vogue body (Fig. 2).

Kanowna Belle

The Kanowna Belle deposit is located on the eastern edge of the Kalgoorlie terrane and the adjacent 'Velvet' discovery is the target of recent mining (Fig. 1). The basal stratigraphy of the Kalgoorlie terrane is composed of tholeiitic and komatiitic mafic-ultramafic rocks, which constitutes the Kambalda Group. Overlying the Kambalda Group is the Kalgoorlie sequence, made up of a complex volcaniclastic succession known as the Black Flag Group (BFG) (Barley et al., 2002; 2003). The Mount Shea porphyry, which intruded into the BFG, has a minimum SHRIMP U-Pb age of 2658±3 Ma (Krapež et al., 2000) and Nd depleted-

mantle model ages (T_{DM}) ranging from 3.10 Ga to 2.95 Ga (Champion and Cassidy, 2007). The locally NE-SW trending Fitzroy fault and the later reactivated faults with NE-SW orientation host the majority of gold mineralization (Wang et al., 2017). The Kanowna Belle deposit is mainly hosted within felsic volcaniclastic rocks and porphyries but rare gold grains are located in fragments of veins, and in altered rocks that form clasts within the BFG volcaniclastic rocks (Fig. 3, Wang et al., 2017).

The summarized geochronological sequence for lithology and gold mineralization ages for the Sunrise Dam and Kanowna Belle is illustrated in Figure 4.

SAMPLING STRATEGY

Granitoid porphyries related to gold mineralization from two giant orogenic gold deposits were collected for lithogeochemical studies. Fresh or minimally altered intrusions were targeted, although nearly all samples are somewhat altered with pervasive white micas (paragonite, muscovite or phengite, Wang et al., 2017). Sample UGD 2419 (proximal to the orebody, Fig. 2) from Sunrise Dam, samples GDD 438 (proximal to the orebody, Fig. 3) and VD10_20 (from the recent Velvet discovery, Fig. 1) from the Kanowna Belle were selected for zircon separation.

ANALYTICAL TECHNIQUES

Lithogeochemical analysis

Fresh samples of igneous rock were prepared by crushing (using corundum plates) and grinding in an agate disk mill. The expected contamination of Si and Al by these methods is estimated to be less than one weight percent (as assessed from analyses of standards and blanks). All samples were analyzed at the LabWest, Perth, Australia. Major elements were

150 analyzed by wavelength dispersive X-ray fluorescence spectrometry. Accuracy for major
151 elements, as determined by reproducibility of standards and duplicates, is typically within
152 five relative percent (< 2 relative % for SiO_2 and Al_2O_3). Trace elements were analyzed with
153 a Finnigan MAT inductively coupled plasma mass spectrometer (ICP-MS, Thermo Scientific
154 X Series 2). Analytical accuracy for most trace elements is better than five relative percent.
155

156 **Zircon U-Pb dating**

157 Zircons were separated from 2–3 kg of crushed rock samples by heavy-liquid and
158 magnetic methods followed by hand-picking at the Hebei Geological Survey Laboratory,
159 China. Selected crystals were typical of magmatic zircons: euhedral, clear, colorless, devoid
160 of mineral and fluid inclusions, and 50–150 μm in diameter. The zircons were mounted in
161 epoxy and polished to reveal interior grain surfaces. Cathodoluminescence (CL),
162 backscattered electron (BSE), and secondary electron (SE) images were obtained prior to
163 analysis, in order to reveal internal zonation and enhance analytical targeting. Zircon U-Pb
164 dating was firstly scrutinized using laser ablation inductively coupled plasma mass
165 spectrometry (LA-ICPMS), at the GeoHistory Facility, John de Laeter Centre, Curtin
166 University, Perth, Australia. The zircons with concordant results from LA-ICPMS were
167 selected for further SHRIMP dating with higher precision.

168 LA-ICP-MS data collection for both ages and trace element abundance was performed
169 simultaneously at the GeoHistory Facility in the John de Laeter Centre, Curtin University,
170 Perth, Australia. Individual zircon grains (mounted and polished in 1" epoxy rounds) were
171 ablated using a Resonetics RESOlution M-50A-LR, incorporating a Compex 102 excimer
172 laser, with a 33 μm diameter laser spot, 7 Hz laser repetition rate, and laser energy of 1.5 J
173 cm^{-2}. Isotopic intensities were measured using an Agilent 7700s quadrupole ICP-MS. Two
174 cleaning pulses were fired before 10 s of background analysis, 30 s of ablation and a further

10 s of baseline signal collection. The sample cell was flushed with ultrahigh purity He (350 mL min^{-1}) and N_2 (3.8 mL min^{-1}) and high purity Ar was employed as the plasma carrier gas (flow rate 0.98 L min-1). For this work ^{28}Si, ^{29}Si, ^{31}P, ^{91}Sr, ^{39}K, ^{44}Ca, ^{45}Sc, ^{49}Ti, ^{57}Fe, ^{71}Ga, ^{85}Rb, ^{88}Sr, ^{89}Y, ^{90}Zr, ^{93}Nb, ^{133}Cs, ^{137}Ba, ^{139}La, ^{140}Ce, ^{141}Pr, ^{146}Nd, ^{147}Sm, ^{151}Eu, ^{157}Gd, ^{159}Tb, ^{163}Dy, ^{165}Ho, ^{166}Er, ^{169}Tm, ^{172}Yb, ^{175}Lu, ^{178}Hf, ^{181}Ta, ^{202}Hg, ^{204}Pb, ^{206}Pb, ^{207}Pb, ^{208}Pb, ^{232}Th, and ^{238}U were monitored for 0.01 s each. Given our inability to correct for the double charged ^{90}Zr interference on ^{45}Sc, data was not utilized for this element. For trace element analysis, international glass standard NIST 610 was used as the primary standard to calculate most elemental concentrations (using ^{29}Si as the internal standard element and assuming 14.76% Si assumed in zircon) and to correct for instrument drift. Hf abundances were determined against zircon GJ-1 (Liu et al., 2010) assuming 43.14% ^{90}Zr in unknowns. Secondary standard NIST 612 was analyzed as an unknown and yielded abundances within 4% of recommended values for most elements. The primary geochronology reference material used in this study was GJ-1 (601.92±0.7 Ma; Jackson et al., 2004), with Plešovice treated as a secondary age standard ($^{206}Pb/^{238}U$ age of 339.5±4.2Ma obtained, within uncertainty of recommended value of 337.13±0.37 Ma; Sláma et al., 2008). The time-resolved mass spectra were reduced using the U_Pb_Geochronology4 data reduction scheme in Iolite (Paton et al, 2011 and references therein).

The coupled U-Pb isotopic and trace element analyses by LA-ICPMS have divided zircons into two groups of igneous zircons and hydrothermal fluid modified zircons. We select zircons with concordant results from each group for further U-Pb age dating and trace element analysis. The U–Pb isotopic analyses were performed using the Sensitive High Resolution Ion Microprobe (SHRIMP II) in the John de Laeter Centre, Curtin University, Australia. The OG1 standard was used to monitor instrument induced mass fractionation of $^{207}Pb/^{206}Pb$ ratio (3465 Ma; Stern et al., 2009). The $^{207}Pb/^{206}Pb$ dates (mean age = 3471.3 Ma)

obtained on OG1 zircons during the SHRIMP session matched the $^{207}Pb/^{206}Pb$ standard age within uncertainty and no fractionated correction was warranted. The TEMORA standard with an age of 417 Ma (Black et al., 2004) was used to monitor performance. Analyses of the OG1 standard were interspersed with those of unknown zircon grains during each measurement session. Data processing was carried out using Squid 2 (Wingate and Lu, 2017), and data were plotted with Isoplot 4.15 (Ludwig, 2012). The uncertainty for individual analyses is quoted at the 1σ level, and the errors on weighted mean ages are at the 95% confidence level.

Secondary ion mass spectrometry: O isotope, $^{16}O^{1}H/^{16}O$, Ti and REE

The oxygen isotopic compositions and Ti, REE (La, Ce, Pr, Nd, Sm, Eu, Gd, Dy, Er, Y, and Lu), Y and Hf concentrations were measured using secondary ion mass spectrometry (SIMS) Cameca IMS-1280 at the Centre for Microscopy, Characterisation and Analysis (CMCA), University of Western Australia. The polished sample mount was coated with 30 nm Au and analyses were performed after polishing to remove the previously measured spots. Although these REE elements have already been measured by LA-ICPMS, La and Pr are very low in abundance and cannot be accurately measured by LA-ICPMS. Therefore, we conduct the REE analysis on representative zircons via SIMS.

SIMS $^{16}O^{1}H/^{16}O$

The *in-situ* oxygen isotopic ratio ($^{18}O/^{16}O$) was measured together with $^{16}O^{1}H/^{16}O$. The sample mount was outgassed inside the 1280 storage under vacuum for three days prior to the analyses to get as low an OH background as possible. A ca. 3 nA focused Cs^{+} primary beam was operated at 10 kV and the secondary ion beam was extracted at -10 kV. The analysis area was pre-sputtered using a 20 × 20 μm raster for 40 seconds followed by automated secondary

centering in the field aperture (FA; 4000 μm) and entrance slit (ES; 60 μm). The analysis used a 15 μm raster employing dynamic transfer at a 130 × field magnification for 12 × 4 second integrations. Two oxygen isotopes and OH were measured simultaneously in mono-multi mode: multicollector Faraday Cup (FC) detectors with amplifiers of 10^{10} and 10^{11} Ω resistor collected ^{16}O and ^{18}O, respectively, and a mono-axial FC with an amplifier of 10^{11} Ω resistor collected OH. Exit slits of 500 and 200 μm were used on each of the multicollector detectors, providing a nominal mass resolving power (MRP) of ca. 2500 and 6000 (^{17}O is resolved from OH with this MRP), respectively. The magnetic field was regulated using nuclear magnetic resonance (NMR). A normal incidence electron gun was used for charge compensation in all analyses. Typical ^{16}O count rate was > 2×10^9 cps. Bracketing of standards permits instrumental mass fractionation (IMF) and drift to be assessed and corrected. IMF was corrected using Geostandard 91500 (Widenbeck et al., 2004). The external reproducibility was 0.31 ‰ (2 sd). Corrected $^{18}O/^{16}O$ ratios are reported in $\delta^{18}O$ notation, in per mil variations relative to Vienna standard mean ocean water (VSMOW). The accuracy of the O isotopic analysis in this study can be assured as we measured secondary zircon standards (Temora 2 and Penglai) during the other sessions before and after this measurement, which yielded the accurate reference values within uncertainty. It also agrees to the long-term zircon oxygen measurement results in the CMCA IMS-1280 lab.

Ti

Titanium concentration was measured using a similar analytical method as described by Kenny et al (2016), as summarized below. A ca. 7 nA projected O_2^- primary beam (ca. 20 um in diameter) was operated at -13 kV and the secondary ion beam was extracted at 10 kV. The analysis area was pre-sputtered using a 25 μm raster for 90 seconds followed by automated

250 secondary centering in the field aperture (FA; 4000 μm), energy centering and mass
251 calibration scanning. Entrance and exit slits of 60 and 400 um (MRP ca. 3000) were used
252 with a 130 × field magnification. ^{49}Ti was analyzed because ^{46}Ti, ^{47}Ti, ^{48}Ti and ^{50}Ti have
253 interferences or possible interferences. Two silicon isotopes (^{28}Si and ^{30}Si) were collected,
254 with the former used for beam centering and the latter used to normalize the Ti signal. Using
255 magnet peak jumping, the axial FC2 with the 10^{11} Ω resistor and electron multiplier (EM)
256 measured ^{28}Si, and ^{30}Si and ^{49}Ti, respectively, for 12 cycles. NIST610 glass (434 ± 18 ppm,
257 Pearcer et al., 1997) was analyzed as the reference material to calibrate Ti concentration, and
258 91500 (5.2 ± 1.5 ppm, Fu et al., 2008; 5.0 ± 0.2 ppm, Kenny et al. 2016) as the secondary
259 standard to monitor the accuracy of the session. No post-analysis correction for the difference
260 in matrix between NIST610 and 91500 was required with -45 eV energy offset applied (30
261 eV energy window and 5 eV gap). The external reproducibility for 91500 was <0.5 % (1 sd;
262 4.5 ± 0.2 ppm).
263
264 *Rare Earth Element Content*
265 Eleven REE (La, Ce, Pr, Nd, Eu, Sm, Gd, Dy, Er, Yb, and Lu), together with Y and Hf,
266 were measured using a similar analytical method as that described in detail by Whitehouse
267 (2004), as summarized below. A ca. 6 nA projected O_2^- primary beam (ca. 20 um in diameter)
268 was operated at -13 kV and the secondary ion beam was extracted at 10 kV. The analysis area
269 was pre-sputtered using a 25 μm raster for 60 seconds followed by automated secondary
270 centering in the field aperture (FA; 4000 μm; 130 × field magnification used), energy
271 centering and mass calibration scanning. As REE concentration levels are quite low (in
272 particular for the trivalent light REEs (LREE; La, Pr, Nd, Sm), all species were collected
273 using EMs (low-noise, ion-counting) and their backgrounds and yields were carefully
274 measured prior to the session. Six LREEs were measured simultaneously using the mono-

axial EM (^{144}Nd; axial exit slit 800 um; MRP ca. 1500) and multicollector EMs (^{139}La, ^{140}Ce, ^{141}Pr, ^{152}Sm, ^{153}Eu; multicollector exit slit 250 um; MRP ca. 4500) with -45 eV energy offset applied (30 eV energy window and 5 eV gap). The multicollection detector background level is significantly low, less than 0.01 cps: the L2 and C detectors collecting La and Pr had the background count rates of 0.002 and 0.008 cps in particular. The other REEs, Y, Hf, the matrix reference ^{30}Si (used to normalize the REE signals) and the mass peak reference $^{90}Zr^{28}Si^{16}O_2$ were analyzed using the axial-EM in the magnet peak jumping mode, and the energy offsets were applied differently for each species according to Whitehouse (2004). Eight cycles were run for an individual analysis. Similar to the Ti measurements, NIST610 glass was analyzed as the reference material to calibrate REEs concentration, and 91500 as the secondary standard to monitor the accuracy of the session. No post-analysis correction for the difference in matrix between NIST610 and 91500 was required.

ANALYTICAL RESULTS

Whole-rock geochemical results

All granitoids have SiO_2 contents between 58.68 and 70.30 wt. % (Table 1). The Kanowna Belle intrusions plot in the quartz diorite to granite fields while the Velvet porphyries show more compositional variation, plotting as syeno-diorite, quartz diorite, and granite. The Sunrise Dam porphyry is granitic in composition (Fig. 5A) with calc-alkaline K_2O contents. The Kanowna Belle and Velvet porphyries are calc-alkaline to high K calc-alkaline (Fig. 5B), while all samples have relatively high Sr/Y ratios (36–169) and La/Yb (36–69) (Fig. 5C, D), plotting in the adakitic field. All samples show significant enrichments of LREE relative to heavy REE (HREE) on chondrite-normalized diagrams (Fig. 6A). They also show relative depletions in Nb, Ta, P, and Ti, and enrichments in Rb, Ba, Th, U, K, Pb, Zr, and Hf on a primitive mantle-normalized trace element diagrams (Fig. 6B), similar to arc-related igneous

rocks worldwide (Perfit et al., 1980; Pearce, 1982; Arculus and Powell, 1986) and post-collisional adakite-like (high-Sr/Y) granitoids in Gangdese belt of southern Tibet (Wang et al., 2014, 2015; Fig. 6). Most sample have weakly negative Eu anomalies (0.70–0.96, Fig. 6A).

LA-ICPMS U-Pb dating and trace element results

Three samples were selected for LA-ICPMS U-Pb, and the results are listed in Table A1 and illustrated in Fig. A1.

Zircons have been divided into four groups based on the results. Analyses >10% discordant or high common-Pb (f204>1%) are Group D (unreliable analyses); analyses <10% discordant can be divided into three groups including Group I of igneous zircons (the main group), Group X of xenocrystic zircons, and Group P of radiogenic Pb loss (those <10% discordant but younger than Group I). The weighted average $^{207}Pb/^{206}Pb$ ages for the Group I of UGD 2419, GDD 438, and VD10_20 are 2677 ± 29 Ma, 2685 ± 34 Ma, 2703 ± 13 Ma, respectively.

The coupled trace element data obtained by LA-ICPMS for zircons from the three samples are reported in digital appendix Table A1. The Group I zircons show typical magmatic features. The hydrothermal fluid modified zircons with younger ages (Group P) or radiogenic Pb loss (Group D) incline to have flat REE patterns, and higher La contents.

SHRIMP U-Pb dating and SIMS trace element results

The zircons with concordant results from LA-ICPMS were selected for further SHRIMP dating with higher precision. Three samples were selected for SHRIMP U-Pb dating, and the results are listed in Table A2. Following the similar grouping criteria to LA-ICPMS dating results, zircons have been divided into four groups based on the results. Analyses >5 % discordant or high common-Pb (f204>1%) are Group D (unreliable analyses); analyses <5 %

discordant can be divided into three groups including Group I of igneous zircons (the main group), Group X of xenocrystic zircons, and Group P of radiogenic Pb loss (those <5 % discordant but younger than Group I).

Sample UGD2419 was collected from a granite porphyry in the Sunrise Dam deposit. This sample also contains a wide range of ages (Fig. 7A), and therefore no concordia intercept age was obtained. The weighted average $^{207}Pb/^{206}Pb$ age for the Group I is 2654 ± 25 Ma, and the rest of grains are scattered between 2660 Ma and 2239 Ma (Fig.8A–C). Sample GDD 438 was collected from the Kanowna Belle granite porphyry. This sample contains several populations of zircons (Fig. 7B), and therefore no concordia intercept age was obtained. The weighted average $^{207}Pb/^{206}Pb$ age for the Group I is 2678 ± 6.6 Ma (Fig. 8D–F), and several grains show ages as young as 2263 Ma (Fig. 7B). Sample VD10_20 was collected from a granite porphyry in the Velvet mine adjacent to Kanowna Belle. This sample contains several populations of zircons with a range of ages (Fig. 7C), and therefore no concordia intercept age was obtained. The weighted average $^{207}Pb/^{206}Pb$ age for the Group I is 2675 ± 6.6 Ma, and the other Groups P + D are centered on 2280Ma and 2480 Ma, respectively (Fig. 7C). All analyzed zircon grains show similar age distributions, including a main population group around 2680 Ma and four post-magmatic groups (Fig. 7D).

Although REE and Ti element have already been measured by LA-ICPMS, La and Pr are very low in abundance and cannot be accurately measured by LA-ICPMS. In addition, SIMS analysis applied a smaller 15 spot size, which avoids the mixing of igneous core and hydrothermal fluid modified rim during the analysis. Trace element data obtained by SIMS for zircons from the three samples are illustrated on Figures 9, 10 and reported in digital appendix Table A2. Some zircon grains show positive chondrite-normalized Ce anomalies, small to significant negative Eu anomalies, and enrichments in heavy rare earth elements (HREEs; Fig. 9), which are typical of igneous zircons (Hoskin and Schaltegger, 2003; Lu et

al., 2016). However, some grains have no chondrite-normalized Ce and Eu anomalies, flat REE patterns with weak enrichment of HREEs compared to LREES, typical of hydrothermal zircons (Pelleter et al., 2007). These grains are free of fluid inclusions, and the previous LA-ICPMS trace element analysis shows no evidence of apatite and fluid inclusions. Since all these zircon grains have typical igneous concentric zoning and generally lack of fluid inclusions, they are more likely hydrothermal fluid modified zircons.

Comparison of zircon LA-ICPMS and SIMS trace element data

Although zircon LA-ICPMS trace element data have shown the large difference of group I zircons from groups P and D, SIMS data show better grouping. With application of LA-ICPMS (45 um spot size), there are signifcant overlaps of REE patterns (Fig. 9A, C, and E) and trace element plots (Fig. 10A, C, E, G) of igneous zircons and hydrothermal fluid modified zircons. The overlaps are likely caused by mixture of igneous zircon core and hydrothermal fluid altered rims during analysis. In addition, the poor analysis on elements with low abundance, such as La and Pr, can lead to the overlaps. For these reasons, we applied the trace element analysis with SIMS because of smaller spot size of 15 um and better precision for La and Pr. The new data of group I zircons show more concentrated and homogeneous geochemical compositions (Figs. 9B, D, F; 10B, D, F). The groups P and D zircons suffered from hydrothermal alteration show much higher La contents, high Eu/Eu* ratios, and lower $(Sm/La)_N$ and Ce/Ce* ratios than Group I zircons.

Zircon O isotopic compositions and $^{16}O^{1}H/^{16}O$ contents

Zircon O isotopic and OH results from this study are listed in Tables A3, and are illustrated in Figure 11.

All three samples show a similar range of zircon O isotopic compositions. Sample GDD 438 has zircon $\delta^{18}O$ values between +3.4 ‰ and +5.9 ‰. Sample VD10_20 has zircon $\delta^{18}O$ values between +4.7 ‰ and +6.3 ‰. Sample UGD2419 has zircon $\delta^{18}O$ values between +3.8 ‰ and +6.1 ‰. In contrast, their OH contents are different with 0.00031–0.00579 for GDD 438, 0.00029–0.00327 for VD10_20, and 0.00031–0.01024 for UGD2419.

DISCUSSION

Geochronology

Previous studies have demonstrated the challenge in correctly dating felsic porphyries in the Eastern Goldfield Province (Ross et al., 2004). The zircons in these rocks commonly have high-U and are metamict, while xenocrysts are common, and many zircons have overgrowth and recrystallization patterns. Without BSE and CL imaging to aid in identification of zircon xenocrysts or overgrown rims, many grains would have been mistaken for magmatic zircons. A cautionary approach to interpreting zircon ages from Eastern Goldfield Province is critical.

Previous dating work has constrained granitic magmatism in the Eastern Goldfields Province to between 2720 and 2630 Ma (Ross et al., 2004 and references therein). Zircon xenocrysts are common in the granitoid rocks, and their ages are normally > 2.69 Ga with some > 2.9 Ga (Hill and Campbell, 1993; Nelson, 1997). The main episode of gold mineralization in the Yilgarn Craton is between 2650 and 2625 Ma (Groves et al., 2000, 2003)

The Dolly porphyry in the Sunrise Dam mine yielded a SHRIMP II U-Pb age of 2674±3 Ma (Brown, 2002). The mineralization ages were inferred from several radiometric systems (Fig. 4), including a molybdenite Re-Os age of 2663±11 Ma, Cr-mica Ar-Ar age of 2667±8 Ma (from the Sunrise Shear Zone), and a hydrothermal xenotime and monazite

SHRIMP II U-Pb age of 2654±8 Ma (from Western Shear Zone; Brown, 2002). Lamprophyre dykes postdate gold mineralization (phlogopite Ar-Ar age of 2080±4 Ma; Brown, 2002). The porphyritic intrusion collected from this study gives a weighted mean $^{207}Pb^*/^{206}Pb^*$ age of 2654 ± 25 Ma, which is slightly younger than previously obtained ages. This sample shows a variety of young ages from 2660 to 2220 Ma, suggesting several complicated hydrothermal or metamorphic events after formation. These young zircons are characterized by high U (>250 ppm) and high La (>0.1 ppm) contents.

The felsic volcaniclastic unit at Kanowna Belle yields a SHRIMP U-Pb age of 2668±9 Ma, with xenocrystic zircons with ~2.68, 2.70 and 2.71 Ga (Ross et al., 2004; Wang et al., 2017). A sample of the mineralized Kanowna Belle porphyries gives a weighted mean $^{207}Pb^*/^{206}Pb^*$ age of 2655±6 Ma (Ross et al., 2004), which is considered to be the maximum age for epigenetic gold mineralization. The main gold mineralization age is constrained by resetting of high-U zircon grains (2.63 Ga) and ore-related Pb-Pb galena (2.63 Ga) (Ross, 2002). In addition, monazite and xenotime from a gold mineralized, altered porphyry give a weighted mean $^{207}Pb^*/^{206}Pb^*$ age of 2640 ±8 Ma (Vielreicher et al., 2015). The main zircon group in sample GDD 438 has a weighted mean $^{207}Pb^*/^{206}Pb^*$ age of 2678 ± 6.6 Ma, which is thought to be the formation age of the porphyritic intrusion. The young grains have high U (>300 ppm) and La (>0.3 ppm) contents (Table A1, A2), typical characteristics of hydrothermal zircons. We can name them as hydrothermal fluid modified zircons because all these zircon grains have typical igneous concentric zoning. The recently discovered Velvet mine is adjacent to Kanowna Belle, and no ages have been reported to date. Sample VD10_20 has several xenocrystic zircons with ages of ~2.8 Ga, and the main group has a weighted mean age of 2678 Ma, similar to the porphyries at Kanowna Belle. More young grains are found in the Velvet porphyries. They are characterized by high U (>300 ppm) and La (>1 ppm) contents, similar to zircons from the Kanowna Belle porphyries. The ages of

these hydrothermal fluid modified zircon grains suggest that hydrothermal alteration postponed the crystallization of porphyries, and lasted until ~2260 Ma.

The hydrothermal fluid modified zircons show a complicated range of ages. Although it might suggest that several fluid pulses occurred after porphyry emplacement, the scatter of these younger ages may simply indicate variable degrees of ancient radiogenic Pb loss. The main stages are identified at ~2600 Ma, 2500 Ma, 2400 Ma, 2350 Ma, and 2250 Ma, however it is not possible to link a particular fluid pulse with the timing of gold mineralization.

Petrogenesis

Granitoid plutons from Kanowna Belle and Sunrise Dam have calc-alkaline to high-K calc-alkaline (rare shoshonitic), syeno-dioritic, quartz dioritic, and granitic compositions (Fig. 5A, B). They have high Sr/Y and La/Yb ratios (Fig. 5C, D) and pronounced, steep normalized REE patterns from high LREE to low HREE (Fig. 6A). On a primitive mantle-normalized trace element diagram, these samples show relative depletions in Nb, Ta, P, and Ti, and enrichments in Th, U, Pb, and K (Fig. 6B). They are classified as tonalite-trondhjemite-granodiorite (TTG) given the high-Sr/Y and La/Yb ratios, intermediate to felsic (> 65 wt. % SiO_2), high Na_2/K_2O (0.55–1.87) ratios, and Nd-Ta negative anomalies. They are high-Al TTGs because Al_2O_3 values are > 15 wt. % at 70 wt. % SiO_2 (Champion or Smithies, 2003). These intrusive rocks can be simply named as “potassic high-Sr/Y granites” (Lu et al., 2018).

The origin of these high-Sr/Y granitoids is restricted to either slab melting or melting in thickened crust. Slab melting has been proposed by numerous authors (e.g. Martin, 1986) to accommodate high pressure and basaltic source. The modern analogues are adakitic rocks (Kay, 1978; Drummond and Defant, 1990, 1996; Martin, 1999). However, experimental evidence, low Mg# and high SiO_2 content, and high K contents are consistent with melting in

449 thickened crust (Rapp et al., 1991; Smithies, 2000). The modern analogues are post-
450 collisional high-Sr/Y granitoids in southern Tibet (Hou et al., 2004; Wang et al., 2014, 2015),
451 as they have a similar trace element distribution (Fig. 6). The $Mg^{\#}$ of granitoid plutons at
452 Kanowna Belle and Sunrise Dam are mostly between 43.1 and 59.1, with the exception of
453 except one sample with a value of 74.1. Such $Mg^{\#}$ values are much lower than those of the
454 adakites from the Aleutian and Cook Islands. In addition, they have higher K_2O contents
455 (2.16–5.16 wt. %). These features suggest they were derived from partial melts in thickened
456 crust, similar to the high-Sr/Y granitoids in southern Tibet (Hou et al., 2004; Wang et al.,
457 2014, 2015). In addition, similar to zircons from high-Sr/Y granitoids in southern Tibet, the
458 magmatic zircons from these Archaean granitoids have intermediate $\delta^{18}O$ values (+5‰ to
459 +6.3‰). These features suggest the Archaean lower crust was newly formed, and therefore
460 the primary magmas have $\delta^{18}O$ values similar to those of the mantle (+5.3±0.3 ‰; Valley et
461 al., 1998). Subsequent mixing and contamination during magma emplacement would elevate
462 the $\delta^{18}O$ values up to +6.3‰. The estimated magmatic crystallization temperatures (Ti-in-
463 zircon) are all below 800°C. The consistently low temperatures for these Archaean granitoids
464 requires additional water-fluxed melting (cf. Lu et al., 2015; Weinberg and Hasalová, 2015;
465 Collins et al., 2016; Wang et al., 2018), because dehydration melting of the crust requires
466 temperatures of at least 850°C to generate reasonable granitic magma volumes.
467

468 **Hydrothermal fluid modified zircons and post-magmatic fluids**

469 Most hydrothermal zircons can be identified based on hydrothermal mineral inclusions
470 or a spongy texture (Kerrich and King, 1993). However, for hydrothermal fluid modified
471 zircons, textural evidence is insufficient to distinguish them from magmatic zircons. Most
472 exhibit oscillatory zoning, and are similar to magmatic zircons. The age of magmatic and
473 hydrothermal fluid modified zircons is indistinguishable, as the latter can be precipitated

from a fluid evolved from the magma during the final stages of crystallization (Hoskin, 2005). Trace-element compositions such as REE patterns of zircons are not indicative of geological environment (Pettke al., 2005; Fu et al., 2009), although the hydrothermal zircons commonly have flat REE patterns with low $(Sm/La)_N$ ratios (Hoskin, 2005).

$\delta^{18}O$ signatures of igneous zircons are generally above +5.5 ‰ (Bindeman and Valley, 2001). Zircons with values below +5.5 are commonly thought to have been formed in the presence of, or exchanged with, surface water or high temperature fluid (Bindeman and Valley, 2001). Most of igneous zircons from this study have relatively homogeneous $\delta^{18}O$ ratios between +5 to +6 (Fig. 11A). In contrast, the low-O zircons (+5 to +3) are associated with high La and OH contents. For example, one grain in sample GDD 438 with low $\delta^{18}O$ has high La_N content (up to 43.7) and some grains have high OH content (up to 5.8×10^{-3}). These features suggest that additional water has been involved in the formation of zircon. The weathering of zircons can significantly lower the $\delta^{18}O$ values to less than 1% (Trail et al., 2007; Pidgeon et al., 2013). However, no zero age discordia intersection for U-Pb analyses is observed in our samples (Fig. 8). Therefore, we suggest the change in $\delta^{18}O$ is related to high temperature fluid alteration and that these zircons should be called "hydrothermal fluid modified zircons". They show distinct REE patterns with flat LREE, and weak Ce and Eu anomalies, in contrast to igneous zircons. The magmatic zircons have higher $\delta^{18}O$ ratios (>5), low La contents (< 1 ppm), low OH contents ($<0.5 \times 10^{-3}$), and relatively homogeneous T (ti-zr) (650–800°C). In contrast, the hydrothermal fluid modified zircons have low and variable $\delta^{18}O$ ratios (3–5), high La contents (1 to 60 ppm), high OH contents ($>0.5 \times 10^{-3}$), and more scattered T (ti-zr) (550–950°C). The Ti-in-zircon thermometer applied to hydrothermal zircons has little geological significance as such temperature estimates are inaccurate.

Three distinct mechanisms have been proposed for the formation of hydrothermal-fluid modified zircon: (i) dissolution-precipitation, documented for high-pressure/low-temperature

meta-igneous rocks (Tomaschek et al., 2003; Van Lankvelt et al., 2016); (ii) ion-exchange during weathering (low-temperature 120 to 200°C) with percolating water reacting with the metamict zircon structure (Pidgeon et al., 2013, 2017); and (iii) direct crystallization by a zircon-saturated fluid (Hoskin, 2005). Low-temperature weathering is not considered here, because near-zero age discordance was not observed in our samples (Fig. 8), similar to Jack Hills (Pidgeon et al., 2017). Dissolution-precipitation textures were not observed in these zircons (Fig. A2–A4), so it is likely that the studied hydrothermal fluid modified zircons crystallized from post-magmatic fluids saturated in Zr and Ti.

Ce^{4+}/Ce^{3+} ratios and Eu_N/Eu_N* ratios have been used to distinguish relatively oxidized, ore-bearing porphyries (Ce^{4+}/Ce^{3+} mostly > 50 and Eu_N/Eu_N* ratios > 0.5) from more reduced, barren intrusive suites (Ballard et al., 2002; Wang et al., 2014). Eu_N/Eu_N* ratios in zircons are also related to plagioclase crystallization, which preferentially partitions Eu^{2+} relative to Eu^{3+}. In hydrous magmas, plagioclase crystallization has minimal effect on zircon because plagioclase fractionation is suppressed (Dilles et al., 2015; Lu et al., 2016). Igneous zircons are characterized by low La contents, high Ce/Ce* ratios, and low Eu/Eu* ratios, while hydrothermal fluid modified zircons all have high Eu/Eu* ratios (> 0.5) and low Ce/Ce* ratios (<0.5). Low Ce/Ce* ratios might be related to reduced fluid environments, and if so, the Eu/Eu* ratios should be low. Thus, oxidation conditions cannot be the only control on the observed compositions. A reduced, Eu-enriched fluid is necessary for generation of these zircons. Such fluids have been described as high-temperature, Cl-rich and low pH hydrothermal fluids with extremely high Eu anomalies (Pelleter et al., 2007 and references therein). Zircons that grow in the high-Eu fluids would have high Eu/Eu* ratios, which mask the redox effect on zircon. Meteoric fluid is not considered here, because it commonly imparts a negative Eu anomaly (Michard and Albarede, 1986; Michard, 1989) and higher $\delta^{18}O$ ratios.

524

525 **Metallogenic implications**

526 The porphyritic intrusions in Kanowna Belle and Sunrise Dam show similar whole rock
527 geochemistry, zircon O isotopic compositions, and crystallization temperatures as high-Sr/Y
528 granitoids in southern Tibet. This suggests the water-fluxed partial melting of lower crust is
529 common in the Cenozoic and is probably a ubiquitous mechanism for forming TTGs in the
530 Archaean. The partial melts of some regions of the lower crust are fertile, and we suggest that
531 the sulphides and their metals were trapped within the roots of the lower crust given the
532 reduced conditions prevailing from previous magmatism. Water-fluxed partial melting of
533 such sulfide-rich lower crust was capable of forming water-rich magmas and transporting
534 metals, giving rise to PCDs (Richards, 2011; Chiaradia et al., 2012; Wang et al., 2014) and
535 likely, some of the studied Archaean gold deposits (e.g., Mueller et al., 2008).

536 The discovery of hydrothermal fluid modified zircons in Archaean gold deposits has
537 important implications for mineralization. Determining the emplacement age of intrusions
538 and the timing of gold mineralization is a challenge for Archaean gold deposits. Textural
539 evidence cannot distinguish between hydrothermal fluid modified zircons and magmatic
540 zircons, and some hydrothermal fluid modified zircons show similar ages to magmatic
541 zircons. Our investigation of the relationship between zircon O-OH isotopic compositions,
542 trace elements, U-Pb discordance, and zircon textures revealed by CL and BSE imaging
543 demonstrates that the impact of hydrothermal alteration on zircons and can be used to
544 improve the precision of dating magmatic and hydrothermal processes. In addition, the
545 characterization of hydrothermal fluid modified zircons in gold camps can provide a better
546 understanding of the nature of ore-related fluids. In this case, those fluids were high-
547 temperature, Cl-rich and low pH with an extremely high Eu anomaly. Such fluids are
548 common in the eastern Yilgarn goldfields (Groves et al., 2003; Wang et al., 2017).

CONCLUSIONS

Orogenic gold deposits reflect one of the great events of gold metallogeny in Earth's history. However, despite extensive work there is still debate about the source of gold, nature of the fluid(s) and mechanisms of precipitation for these systems. Zircons of ore-related intrusions from the Archaean Kanowna Belle and Sunrise Dam gold deposits (both > 10 Moz) in one of the Australia's preeminent ore district were investigated for O-OH isotopic signatures, trace element abundance, and U-Th-Pb compositions in order to elucidate the nature of the magmatic source and ore-related fluid. Hydrothermal fluid modified zircons are texturally indistinguishable from magmatic zircons, but their trace element, OH, and isotopic compositions are distinct. Magmatic zircons have higher $\delta^{18}O$ ratios (>5), low La contents (< 1 ppm), low OH contents (<0.5 x 10^{-3}), and relatively homogeneous T (ti-zr) (650–800°C). In contrast, the hydrothermal fluid modified zircons have discordant U-Pb ages, low and variable $\delta^{18}O$ ratios (3–5), high La contents (1 to 60 ppm), high OH contents (>0.5 x 10^{-3}), and more scattered T (ti-zr) (550–950°C). Magmatic zircons are interpreted as having crystallized from positive $\delta^{18}O$ magmas during water-fluxed melting of juvenile lower crust. The involvement of hydrothermal fluid in zircon growth is evidenced by a negative correlation between OH content and $\delta^{18}O$. The studied hydrothermal fluid modified zircons were likely related to a high-temperature, Zr-saturated, high-Eu, Cl-rich, and low-pH hydrothermal fluid. Such fluids are common in eastern Yilgarn gold camps.

ACKNOWLEDGEMENT

This research was financially co-supported by the MOST of China (2016YFC0600304 and 2016YFC0600407), the Chinese National Natural Science Foundation (91755207 and 41225006), and the 111 Project (B18048). We thank Jianwei Zi for processing the SIMS U-Pb data, and Bob Pidgeon for insightful comments on an early version. Bradley McDonald is

574 thanked for assistance with LA-ICPMS zircon U-Pb dating and trace element analysis.
575 GeoHistory Facility instruments were funded via an Australian Geophysical Observing
576 System grant provided to AuScope Pty Ltd. by the AQ44 Australian Education Investment
577 Fund program. We also thank Celestine Mercer for handling our manuscript. Dr. Yongjun Lu
578 and the other anonymous reviewer are thanked for constructive reviews.
579

580 **REFERENCES**

581 Arculus, R., and Powell, R. (1986) Source component mixing in the regions of arc magma
582 generation. Journal of Geophysical Research, v. 91, p. 5913–5926.
583 Ballard, J.R., Palin, J.M, and Campbell, I.H. (2002) Relative oxidation states of magmas
584 inferred from Ce(IV)/Ce(III) in zircon: Application to porphyry copper deposits of
585 northern Chile: Contributions to Mineralogy Petrology, v. 144, p. 347–364.
586 Baker, T., Bertelli, M., Blenkinsop, T., Cleverley, J.S., Mclellan, J., Nugus, M., and Gillen,
587 D. (2010) P-T-X conditions of fluids in the Sunrise Dam gold deposit, Western Australia,
588 and implications for the interplay between deformation and fluids: Economic Geology, v.
589 105, p. 873 – 894.
590 Blewett, R.S., Henson, P.A., Roy, I.G., Champion, D.C., and Cassidy, K.F. (2010) Scale
591 integrated architecture of the world-class gold mineral systems of the Archaean Eastern
592 Yilgarn Craton. Precambrian Research, v. 183, p. 230–250.
593 Black, L.P., Kamo, S.L., Allen, C.M., Davis, D., Aleinikoff, J.N., Valley, J.W., Mundil, R.,
594 Campbell, I.H., Korsch, R.J., Williams, I.S., and Foudoulis, C. (2004) Improved $^{206}Pb/^{238}U$
595 microprobe geochronology by the monitoring of a trace-element-related matrix effect;
596 SHRIMP, ID-TIMS, ELA-ICP-MS and oxygen isotope documentation for a series of
597 zircon standards. Chemical Geology, v. 205, p. 115–140.
598 Blewett, R.S., Henson, P.A., Roy, I.G., Champion, D.C., and Cassidy, K.F. (2010) Scale

integrated architecture of the world-class gold mineral systems of the Archaean eastern Yilgarn craton: Precambrian Research, v. 183, p. 230–250.

Brown, S.M., Fletcher, I.R., Stein, H.J., Snee, L.W., and Groves, D.I. (2002) Geochronological constraints on pre-, syn-, and postmineralization events at the world-class Cleo gold deposit, Eastern Goldfields province, Western Australia: Economic Geology, v. 97, p. 541–559.

Cassidy, K.F. (2006) Geological evolution of the eastern Yilgarn craton (EYC), and terrane, domain and fault nomenclature: Geoscience Australia Record 2006/04, p. 1–19.

Claoue-Long, J.C., Compston, W., and Cowden, A. (1988) The age of the Kambalda greenstones resolved by ion-microprobe: Implications for Archaean dating methods. Earth and Planetary Science Letters, v. 89, p. 239–259.

Champion, D.C., and Cassidy, K.F. (2007) An overview of the Yilgarn craton and its crustal evolution: Geoscience Australia Record 2007/14, p. 13–35.

Champion, D.C. and Smithies, R.H. (2001) Archaean granites of the Yilgarn and Pilbara cratons, Western Australia. In K.F. Cassidy, J.M. Dunphy and M.J. Van Kranendonk (editors), 4th International Archaean Symposium 2002, Extended abstracts. AGSO Geoscience Australia, Record 2001/37, 134-136.

Champion, D.C. and Smithies, R.H. (2003) Archaean granites. The Ishihara Symposium. Granites and Associated Metallogenesis, 13–17.

Chiaradia, M. (2014) Copper enrichment in arc magmas controlled by overriding plate thickness: Nature Geoscience, v. 7, p. 43–46.

Collins, W.J., Huang, H.Q., and Jiang, X.Y. (2016) Water-fluxed crustal melting produces Cordilleran batholiths. Geology, v. 2, p. 143–146.

Drummond, M.S. and Defant, M.J. (1990) A model for trondhjemite-tonalite-dacite genesis and crustal growth via slab melting. Archaean to modern comparisons. Journal of

624 Geophysical Research, 95B, 21503-21521.
625 Drummond, M.S., Defant, M.J. and Kepezhinskas, P.K. (1996) Petrogenesis of slab-derived
626 trondhjemite-tonalite-dacite/adakite magmas. Transactions of the Royal Society of
627 Edinburgh, Earth Science, v. 87, p. 205-215.
628 Fu, B., Page, F.Z., Cavosie, A.J., Clechenko, C.C., Fournelle, J., Kita, N.T., Lackey, J.S.,
629 Wilde, S.A., and Valley, J.W. (2008) Ti-in-Zircon thermometry: applications and
630 limitations. Contributions to Mineralogy and Petrology, v. 156, p.197–215.
631 Fu, B., Mernagh, T.P., Kita, N.T., Kemp, A.I.S., and Valley, J.W. (2009) Distinguishing
632 magmatic zircon from hydrothermal zircon: A case study from the Gidginbung high-
633 sulphidation Au-Ag-(Cu) deposit, SE Australia. Chemical Geology, v. 259, p. 131−142.
634 Goleby, B.R., Blewett, R.S., Champion, D.C., Korsch, R.J., Bell, B., Groenewald, P.B.,
635 Jones, L.E.A., Whitaker, A.J., Cassidy, K.F., and Carlson, G.M. (2002) Deep seismic
636 profiling in the NE Yilgarn: Insights into its crustal architecture: Australian Institute of
637 Geoscientists Bulletin, v. 36, p. 63–66.
638 Goldfarb, R.J., and Groves, D.I. (2015) Orogenic gold: Common or evolving fluid and metal
639 sources through time. Lithos, v. 233, p. 2–26.
640 Groves, D.I., Goldfarb, R.J., Knox-Robinson, C.M., Ojala, J., Gardoll, S., Yun, G., and
641 Holyland, P. (2000) Late-kinematic timing of orogenic gold deposits and its significance
642 for computer-based exploration techniques with emphasis on the Yilgarn block, Western
643 Australia. Ore Geology Reviews, v. 17, p. 1–38.
644 Groves, D.I., Goldfarb, R.J., Robert, F., and Hart, C.J.R. (2003) Gold deposits in
645 metamorphic belts: overview of current understanding, outstanding problems, future
646 research, and exploration significance. Economic Geology, v. 98, p. 1–29.
647 Hodkiewicz, P.F., Groves, D.I., Davidson, G.J., Weinberg, R.F., and Hagemann, S. (2009)
648 Influence of structural setting on sulphur isotopes in Archean orogenic gold deposits,

649 Eastern Goldfields Province, Yilgarn, Western Australia: Mineralium Deposita, v. 44, p.
650 129–150.
651 Hou, Z.Q., Gao, Y.F., Qu, X.M., Rui, Z.Y., and Mo, X.X. (2004) Origin of adakitic intrusives
652 generated during mid-Miocene east-west extension in southern Tibet. Earth and Planetary
653 Science Letters, v. 220, p. 139–155.
654 Hoskin, P.W.O., and Schaltegger, U. (2003) The composition of zircon and igneous and
655 metamorphic petrogenesis, in Hanchar, J.M., and Hoskin, P.W.O. eds., Zircon: Reviews in
656 Mineralogy and Geochemistry, v. 53, p. 27–62.
657 Hoskin, P.W.O. (2005) Trace-element composition of hydrothermal zircon and the alteration
658 of Hadean zircon from the Jack Hills, Australia: Geochimica et Cosmochimica Acta, v. 69,
659 p. 637–648.
660 Hill, R.I., and Campbell, I.H. (1993) Age of granite emplacement in the Norseman region of
661 Western Australia. Australian Journal of Earth Sciences, v. 40, p. 559–574.
662 Jackson, S.E., Pearson, N.J., Griffin, W.L. and Belousova, E.A. (2004) The application of
663 laser ablation-inductively coupled plasma-mass spectrometry to in situ U-Pb zircon
664 geochronology. Chemical Geology, v. 211, p. 47–69.
665 Kay, R.W. (1978) Aleutian magnesian andesites: melts from subducted Pacific oceanic crust.
666 Journal of Volcanology and Geothermal Research, v. 4, p. 117–132.
667 Kenny, G.G., Whitehouse, M.J. and Kamber, B.S. (2016) Differentiated impact melt sheets
668 may be a potential source of Hadean detrital zircon: Geology, v. 44, p. 435–438.
669 Kerrich, R., and King, R. (1993) Hydrothermal zircon and baddeleyite in Val d'Or Archean
670 meothermal gold deposits: characteristics, compositions, and fluid-inclusion properties,
671 with implications for timing of primary gold mineralization. Canadian Journal of Earth
672 Sciences, v. 30, p. 2334–2352.
673 Krapež, B., Brown, S.J.A., Hand, J., Barley, M.E., and Cas, R.A.F. (2000) Age constraints on

674 recycled crustal and supracrustal sources of Archaean metasedimentary sequences, Eastern
675 Goldfields Province, Western Australia: evidence from SHRIMP zircon dating:
676 Tectonophysics, v. 322, p. 89–133.
677 Liu, Y.S., Hu, Z.C., Zong, K.Q., Gao, C.G., Gao, S., Xu, J and Chen, H.H. (2010)
678 Reappraisement and refinement of zircon U-Pb isotope and trace element analyses by LA-
679 ICP-MS. Chinese Science Bulletin, v. 55. P. 1535–1546.
680 Lu, Y.J., Loucks, R.B., Fiorentini, M.L., Yang, Z.M., Hou, Z.Q. (2015) Fluid flux melting
681 generated postcollisional high-Sr/Y copper ore-forming water-rich magmas in Tibet,
682 Geology, v. 43, p. 583–586.
683 Lu, Y.J., Loucks, R.R., Fiorentini, M.L., McCuaig, T.C., Evans, N.J., Yang, Z.M., Hou, Z.Q.,
684 Kirkland, C.L., Parra-Avila, L.A., Kobussen, A. (2016) Zircon Compositions as a
685 Pathfinder for Porphyry Cu± Mo ± Au Deposits, Society of Economic Geologists Special
686 Publication 19, p. 329–347.
687 Lu, Y.J., Smithies, R.H., Wingate, M.T.D., Evans, N.J., Morris, P., Champion, D., and
688 McCuaig, T.C. (2018) Zircon composition as fertility indicator of Archean granite,
689 Geological Survey of Western Australia, Record 2018/2, p. 18–23.
690 Ludwig, K.R. (2012) User's Manual for Isoplot 3.75, a Geochronological Toolkit for
691 Microsoft Excel: Berkeley Geochronology Center Special Publication, Berkeley, CA,
692 USA. no. 5 (75 pp.).
693 Martin, H. (1999) Adakitic magmas: modern analogues of Archaean granitoids. Lithos, v. 46,
694 p. 411–429.
695 Michard, A. (1989) REE concentrations in hydrothermal solutions. Geochimica et
696 Cosmochimica Acta 53, 745–750.
697 Michard, A., and Albarede, F. (1986) The REE content of some hydrothermal fluids.
698 Chemical Geology, v. 55, p. 51–60.

699 Mueller, A.G., Hall, G.C., Nemchin, A.A., Stein, H.J., Creaser, R.A., and Mason, D.R.
700 (2008) Archaean high-Mg monzodiorite-syenite, epidote skarn, and biotite-sericite gold
701 lodes in the Granny Smith-Wallaby district, Australia: U-Pb and Re-Os chronometry of
702 two intrusion-related hydrothermal systems: Mineralium Deposita, v. 43, p. 337–362.
703 Nelson, D.R. (1997) Evolution of the Archaean granite–greenstone terranes of the Eastern
704 Goldfields, Western Australia: SHRIMP U–Pb zircon constraints. Precambrian Research,
705 v. 83, p. 57–81.
706 Neumayr, P., Walshe, J.L., and Hagemann, S. (2005) Camp- to deposit-scale alteration
707 footprints in the Kalgoorlie-Kambalda area: pmd*CRC, project Y3, p. 1–100.
708 Nugus, M.J., Biggam, J., Clark, F., and Erickson, M. (2009) Development and application of
709 macroscopic geological proxies for gold mineralization in high nugget environments—an
710 example from the Sunrise Dam gold mine, Western Australia: International Mining
711 Geology Conference, 7th, Perth, WA, 17−19 August 2009, Proceedings, p. 309–318.
712 Paton, C., Hellstrom, J., Paul, B., Woodhead, J. and Hergt, J. (2011) Iolite: freeware for the
713 visualization and processing of mass spectrometer data. Journal of Analytical Atomic
714 Spectrometry, v. 26, p. 2508–2518.
715 Pearce, J.A. (1982) Trace element characteristics of lavas from destructive plate boundaries.
716 In: Thorp, R.S. (Ed.), Andesites. Orogenic Andesites and Related Rocks. John Wiley and
717 Sons, New York (724 pp.).
718 Pearce N.J.G., Perkins W.T., Westgate J.A., Gorton M.P., Jackson S.E., Neal C.R. and
719 Chenery S.P. (1997) A compilation of new and published major and trace element data for
720 NIST SRM 610 and NIST SRM 612 glass reference materials. Geostandards Newsletter:
721 The Journal of Geostandards and Geoanalysis, 21, 115–144.
722 Pelleter, E., Cheilletz, A., Gasquet, D., Mouttaqi, A., Annich, M., El Hakour, A., Deloule, E.,
723 and Féraud, G. (2007) Hydrothermal zircons: A tool for ion microprobe U-Pb dating of

724 gold mineralization (Tamlalt-Menhouhou gold deposit-Morocco). Chemical Geology, v.
725 245, p. 135–161.
726 Perfit, M.R., Gust, D.A., Bence, A.E., Arculus, R.J., and Taylor, S.R. (1984) Chemical
727 characteristics of island arc basalts: implication for mantle sources. Chemical Geology, v.
728 30, p. 227–256.
729 Pettke, T., Audetat, A., Shaltegger, U., and Heinrich, C.A. (2005) Magmatic-to-hydrothermal
730 crystallization in the W–Sn mineralized Mole Granite (NSW, Australia) Part II: Evolving
731 zircon and thorite trace element chemistry. Chemical Geology, v. 220, p. 191–213.
732 Pidgeon, R.T., Nemchin, A.A., and Cliff, J. (2013) Interaction of weathering solutions with
733 oxygen and U-Pb isotopic systems of radiation damaged zircon from an Archaean granite,
734 Darling Range Batholith, Western Australia. Contributions to Mineralogy and Petrology,
735 v. 166, p. 511–523.
736 Pidgeon, R.T., Nemchin, A.A., and Whitehouse, M.J. (2017) The effect of wreathing on U-
737 Th-Pb and oxygen isotope systems of ancient zircons from the Jack Hills, Western
738 Australia. Geochimica Cosmochimica Acta, v. 197, p. 142–166.
739 Rapp, P.R., Watson, E.B. and Miller, C.F. (1991) Partial melting of amphibolite/eclogite and
740 the origin of Archaean trondhjemites and tonalites. Precambrian Research, v. 51, p. 1–25.
741 Richards, J.P. (2011) Magmatic to hydrothermal metal fluxes in convergent and collided
742 margins: Ore Geology Reviews, v. 40, p. 1–26.
743 Ross, A.A. (2002) Genesis of the Kanowna Belle gold deposit, Kalgoorlie, Western
744 Australia: Implications for Archean metallogeny in the Yilgarn craton: Ph.D. thesis,
745 University of Western Australia, 230 p.
746 Ross, A.A., Barley, M.E., Brown, S.J.A., McNaughton, N.J., Ridley, J.R., and Fletcher, I.R.
747 (2004) Young porphyries, old zircons: new constraints on the timing of deformation and
748 gold mineralisation in the Eastern Goldfields from SHRIMP U–Pb zircon dating at the

749 Kanowna Belle Gold Mine, Western Australia. Precambrian Research, v. 128, p. 104–142.
750 Sláma, J., Košler, J., Condon, D.J., Crowley, J.L., Gerdes, A., Hanchar, J.M., Horstwood,
751 M.S.A., Morris, G.A., Nasdala, L., Norberg, N., Schaltegger, U., Schoene, B., Tubrett,
752 M.N. and Whitehouse, M.J. (2008) Plesovice zircon – A new natural reference material
753 for U-Pb and Hf isotopic microanalysis. Chemical Geology, v. 249, p. 1–35.
754 Smithies, R.H. (2000) The Archaean tonalite-trondhjemite-granodiorite (TTG) series is not
755 an analogue of Cenozoic adakite. Earth Planetary Science Letters, v. 182, p. 115–125.
756 Stern, R.A., Bodorkos, S., Kamo, S.L., Hickman, A.H., Corfu, F. (2009) Measurement of
757 SIMS instrumental mass fractionation of Pb isotopes during zircon dating. Geostandards
758 and Geoanalytical Research, v. 33, p. 145–168.
759 Swager, C.P. (1997) Tectono-stratigraphy of late Archaean greenstone terranes in the
760 southern Eastern Goldfields, Western Australia: Precambrian Research, v. 83, p. 11–42.
761 Swager, C.P., Griffin, T.J., Witt, W.K., Wyche, S., Ahmat, A.L., Hunter, W.M., and
762 McGoldrick, P.J. (1995) Geology of the Archaean Kalgoorlie terrane— an explanatory
763 note: Geological Survey of Western Australia Report 48, 26 p.
764 Trail, D., Mojzsis, S.J., and Harrison, T.M. (2007) Thermal events documented in Hadean
765 zircons by ion microprobe depth profile. Geochimica Cosmochimica Acta, v. 71, p. 4044–
766 4065.
767 Tomaschek, F., Kennedy, A.K., Villa, I.M., Lagos, M. and Ballhaus, C. (2003) Zircons from
768 Syros, Cyclades, Greece–-recrystallization and mobilization of zircon during high-
769 pressure metamorphism. Journal of Petrology, v. 44, p. 1977–2002.
770 Valley, J.W., Kinny, P.D., Schulze, D.J., and Spicuzza,M.J. (1998) Zircon megacrysts
771 fromkimberlite: oxygen isotope variability among mantle melts. Contributions to
772 Mineralogy and Petrology, v. 133, p. 1–11.
773 Van Lankvelt, A., Schneider, D.A., Biczok, J., McFarlane, C.R.M., and Hattori, K. (2016)

774 Decoding zircon geochronology of igneous and alteration events based on chemical and
775 microstructural features: a study from the western superior province, Canada. Journal of
776 Petrology, v. 57, p. 1309–1334.
777 Vielreicher, N., Groves, D., McNaughton, N., and Fletcher, I., 2015. The timing of gold
778 mineralization across the eastern Yilgarn craton using U-Pb geochronology of
779 hydrothermal phosphate minerals. Mineralium Deposita, v. 50, p. 391–428.
780 Wang, R., Richards, J.P., Hou, Z.Q., Yang, Z.M., and DuFrane, S.A. (2014) Increased
781 magmatic water content–the key to Oligo-Miocene porphyry Cu–Mo ± Au formation in
782 the eastern Gangdese belt, Tibet. Economic Geology, v. 109, p. 1315–1339.
783 Wang, R., Richards, J.P., Zhou, L.M., Hou, Z.Q., Stern, R.A., Creaser, R.A., and Zhu, J.J.
784 (2015) The Role of Indian and Tibetan lithosphere in spatial distribution of Cenozoic
785 magmatism and porphyry Cu-Mo±Au deposits in the Gangdese belt, southern Tibet.
786 Earth-Science Reviews, v. 150, p. 68–94.
787 Wang, R., Cudahy, T., Laukamp, C., Walshe, J.L., Bath, A., Mei, Y., Young, C., Roache,
788 T.J., Jenkins, A., Clarke, F., Baker, A., Roberts, M., and Laid, J. (2017) White mica as a
789 hyperspectral tool in exploration for Sunrise Dam and Kanowna Belle gold deposits,
790 Western Australia. Economic Geology, v. 112 (5), p. 1153–1176.
791 Wang, R., Weinberg, R.F., Collins, W.J., Richards, J.P., Zhu, D.C. (2018) Origin of post-
792 collisional magmas and formation of porphyry Cu deposits in southern Tibet, Earth-
793 Science Reviews, v. 181, p. 122–143.
794 Weinberg, R.F., and Hasalová, P. (2015) Water-fluxed melting of the continental crust: A
795 review. Lithos, v. 212–215, p. 158–188.
796 Whitehouse, M.J. (2004) Multi-collector SIMS determination of trace lanthanides in zircon.
797 Geostandards and Geoanalytical Research, v. 28, p. 195–201.
798 Wiedenbeck, M., Hanchar, J.M., Peck, W.H., et al. (2004) Further characterization of the

799 91500 zircon crystal. Geostandards and Geoanalytical Research, v. 28, p. 9–39.
800 Wingate, M.T.D. and Lu, Y. (2017) Introduction to geochronology information released in
801 2017: Geological Survey of Western Australia, 5p.
802 Witt, W.K., and Vanderhor, F. (1998) Diversity within a unified model for Archaean gold
803 mineralization in the Yilgarn craton of Western Australia: An overview of the late-
804 orogenic, structurally-controlled gold deposits: Ore Geology Review, v. 13, p. 29–64.
805 Zhou, Q., Jiang, Y.H., Zhao, P., Liao, S.Y., Jin, G.D., Liu, Z., and Jia, R.Y. (2012) SHRIMP
806 U-Pb dating on hydrothermal zircons: Evidence for an Early Cretaceous epithermal event
807 in the Middle Jurassic Dexing porphyry copper deposit, Southeast China. Economic
808 Geology, v. 107, p. 1507–1514.
809
810 Captions:
811 Fig. 1. Map indicating major tectonic units, boundaries, and Kanowna Belle, Sunrise Dam,
812 and Velvet deposits within Yilgarn Craton (modified from Blewett et al., 2010; Wang et al.,
813 2017).
814
815 Fig. 2. North facing, east-west, composite cross section through the Sunrise Dam, showing
816 the key lithologies, shear zones, and mineralized domains (modified after Nugus et al., 2009;
817 Baker et al., 2010; Wang et al., 2017). No vertical exaggeration. The black stepped line is the
818 outline of the open pit.
819
820 Fig. 3. Map indicating major faults, lithology, and gold orebodies and grades in the Kanowna
821 Belle mine (modified from Neumayr et al., 2005 and Wang et al., 2017).
822

823 Fig. 4. Summarized geochronological sequence for lithology and gold mineralization ages for
824 the Sunrise Dam and Kanowna Belle (see Wang et al., 2017 and references therein and this
825 study). Metamorphic events and corresponding time periods (Blewett et al., 2010) are shown
826 as reference. SSZ = Sunrise shear zone, WSZ = Western shear zone.
827
828 Fig. 5. A. Total alkali-silica diagram for granitoids from Kanowna Belle, Velvet, and Sunrise
829 Dam. B. SiO_2 vs. total K_2O. C. Sr/Y ratios vs. Y. D. La/Yb ratios vs. Yb. "Adakite-like rock"
830 field from Defant and Drummond (1990). KB = Kanowna Belle, SD = Sunrise Dam, VD =
831 Velvet drill core.
832
833 Fig. 6. (A) Chondrite- and (B) primitive mantle (PM)-normalized trace element diagrams for
834 samples of granitoids from Kanowna Belle, Velvet, and Sunrise Dam. Normalization values
835 of Sun and McDonough (1989). The shade area is for high-Sr/Y granitoids from Gangdese
836 belt (Wang et al., 2014). KB = Kanowna Belle, SD = Sunrise Dam, VD = Velvet drill core.
837
838 Fig. 7. Zircon SHRIMP U-Pb $^{207}Pb^*/^{206}Pb^*$ age histograms and relative probability curves for
839 granitoids from Sunrise Dam, Kanowna Belle, and Velvet. A. Sample UGD2419. B.
840 Sample GDD 438. C. Sample VD10_20. D. All samples from this study.
841
842 Fig. 8. Zircon SHRIMP U-Pb concordia and weighted mean diagrams for granitoids from
843 Sunrise Dam (A-C), Kanowna Belle (D–F), and Velvet (G–I). Analyses of Group I of
844 magmatic zircons are shown with separately.
845
846 Fig. 9. Chondrite-normalized trace element diagrams for zircons from granitoids of Sunrise
847 Dam, Kanowna Belle, and Velvet using LA-ICPMS (A, C, E) and SIMS (B, D, F).

Fig. 10. Zircon trace element ratio plots for granitoids from Sunrise Dam, Kanowna Belle, and Velvet. A and B. $(Sm/La)_N$ vs. La. C and D. Ce/Ce* vs. La. E and F. Eu/Eu* vs. La. G and H. Eu/Eu* vs. Ce/Ce*. Here figures A, C, E, G are from LA-ICPMS data and B, D, F, and H are from SIMS data. The shade fields corresponding to the magmatic and hydrothermal fields described by Hoskin (2005). The cycled field is for Group I of magmatic zircons from this study.

Fig. 11. Plots of zircon SIMS trace element, O isotopes, and temperatures estimates for granitoids from Sunrise Dam, Kanowna Belle, and Velvet. A. $\delta^{18}O$ vs La, B. $^{16}O^{1}H/^{16}O$ (10^{-3}) vs La, C. $\delta^{18}O$ vs $^{16}O^{1}H/^{16}O$ (10^{-3}), and D. T (ti-zr) °C vs La.

Tables

Table 1 Major and trace element compositions of granitoids from Sunrise Dam, Kanowna Belle, and Velvet.

Appendix

Fig. A1. Zircon LA-ICPMS U-Pb concordia and weighted mean diagrams for granitoids from Sunrise Dam (A-C), Kanowna Belle (D–F), and Velvet (G–I). Analyses of Group I of magmatic zircons are shown with separately.

Fig. A2. BSE images of representative analyzed zircons of granitoids from Sunrise Dam (UGD2419) and showing in situ U-Pb ages (Purple dashed circle for LA-ICPMS, red circle for SIMS), O isotope/ $^{16}O^{1}H/^{16}O$ (10^{-3}) (yellow cycle), Ti content (blue cycle), and

La content (white square).

Fig. A3. BSE images of representative analyzed zircons of granitoids from Kanowna Belle (GDD 438), and showing in situ U-Pb ages (Purple dashed circle for LA-ICPMS, red circle for SIMS), O isotope/ $^{16}O^{1}H/^{16}O$ (10^{-3}) (yellow cycle), Ti content (blue cycle), and La content (white square).

Fig. A4. BSE images of representative analyzed zircons of granitoids from Velvet (VD10_20), and showing in situ U-Pb ages (Purple dashed circle for LA-ICPMS, red circle for SIMS), O isotope/ $^{16}O^{1}H/^{16}O$ (10^{-3}) (yellow cycle), Ti content (blue cycle), and La content (white square).

Table A1 Zircon U-Pb SHRIMP analytical data for granitoids from Sunrise Dam, Kanowna Belle, and Velvet.

Table A2 Zircon U-Pb LA-ICPMS analytical data for granitoids from Sunrise Dam, Kanowna Belle, and Velvet.

Table A3 Zircon SIMS REE, Ti, and O/OH compositions of granitoids from Sunrise Dam, Kanowna Belle, and Velvet.

898

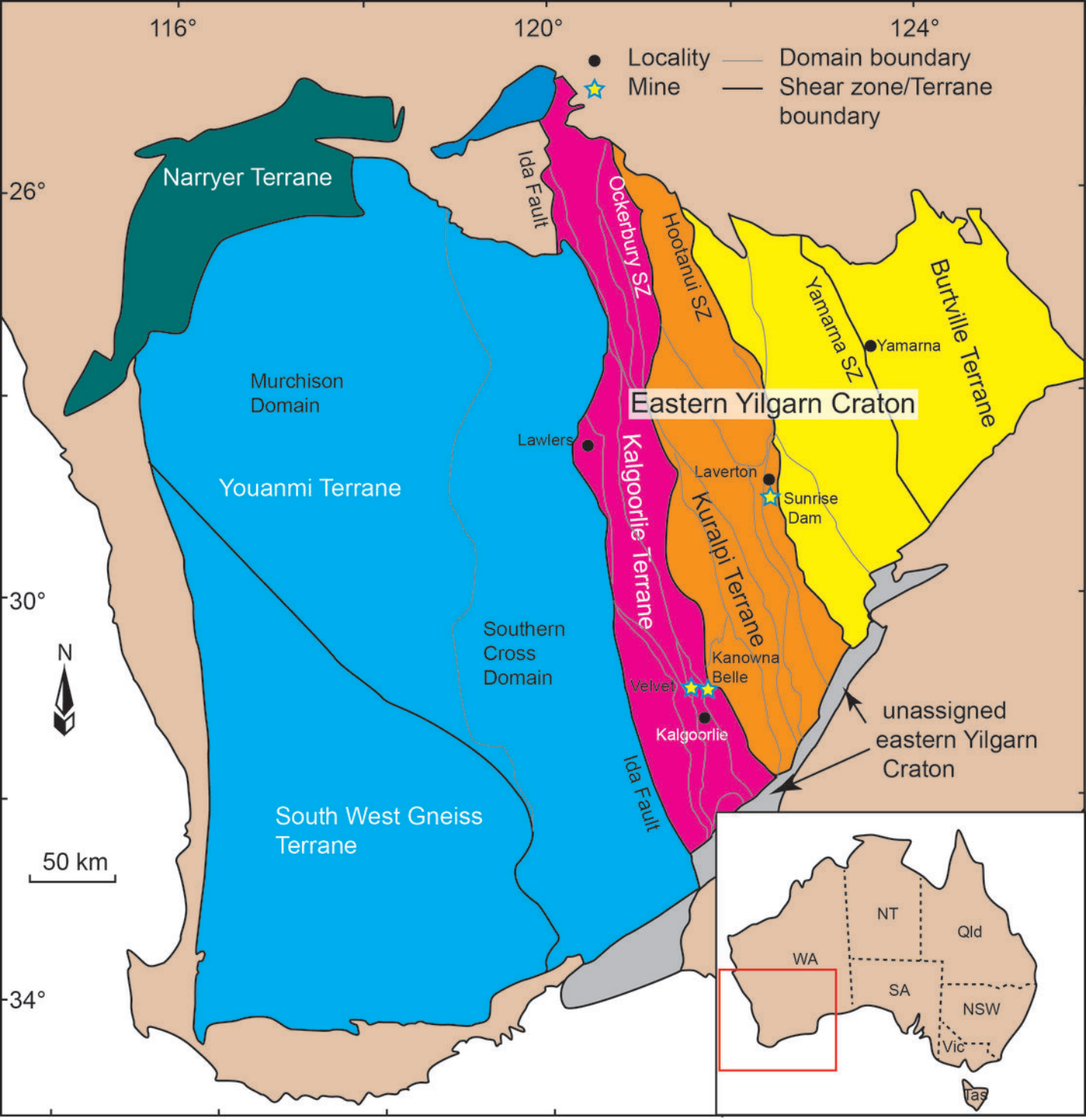
116°
120°
124°
26°
30°
34°
Locality
Mine
Domain boundary
Shear zone/Terrane boundary
Narryer Terrane
Ida Fault
Ockerbury SZ
Hootanui SZ
Yamarna SZ
Burtville Terrane
Yamarna
Eastern Yilgarn Craton
Murchison Domain
Lawlers
Youanmi Terrane
Kalgoorlie Terrane
Kuralpi Terrane
Laverton
Sunrise Dam
Southern Cross Domain
Kanowna Belle
Velvet
Kalgoorlie
Ida Fault
unassigned eastern Yilgarn Craton
South West Gneiss Terrane
N
50 km
NT
Qld
WA
SA
NSW
Vic
Tas

Fig. 1

W

E

GU shear zone

Western shear zone

Watu

Mako 1

Mako 2

Sunrise shear zone

GQ2

GQ

Doly

Hammerhead

Midway shear zone

Cosmo

Hammerhead shear zone

Carey shear zone

Vogue

200 m

Breccia lodes

Major shear zones

Granite

Sampling location

Porphyritic syenite and dikes

Basalt & dolerite sills

BIF-dominated sediments

Volcanic conglomerate

Turbidite beds (no BIF)

Andesite lavas & domes

Fig. 2

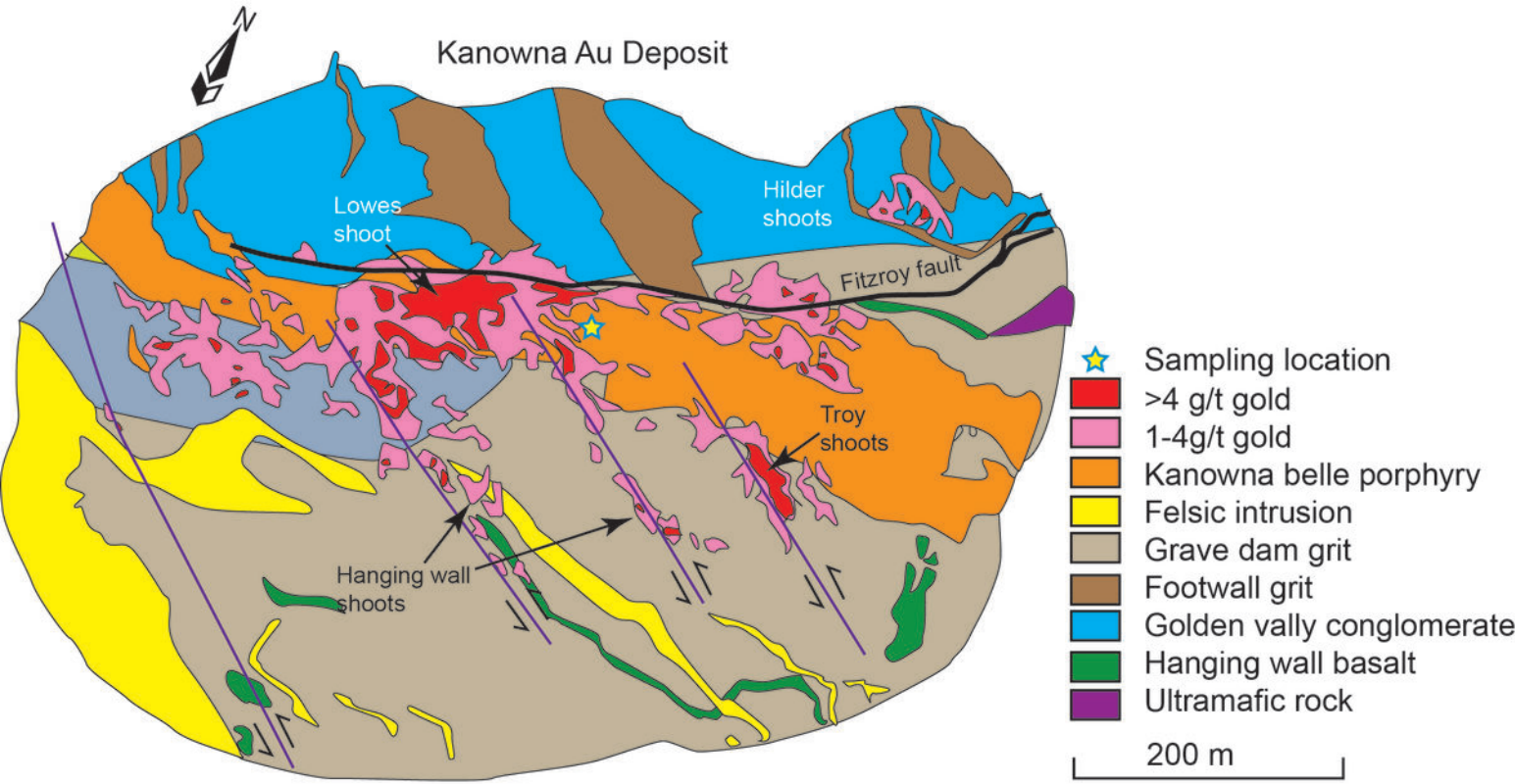
Kanowna Au Deposit
N
Lowes shoot
Hilder shoots
Fitzroy fault
Troy shoots
Hanging wall shoots
Sampling location
>4 g/t gold
1-4g/t gold
Kanowna belle porphyry
Felsic intrusion
Grave dam grit
Footwall grit
Golden vally conglomerate
Hanging wall basalt
Ultramafic rock
200 m

Fig. 3

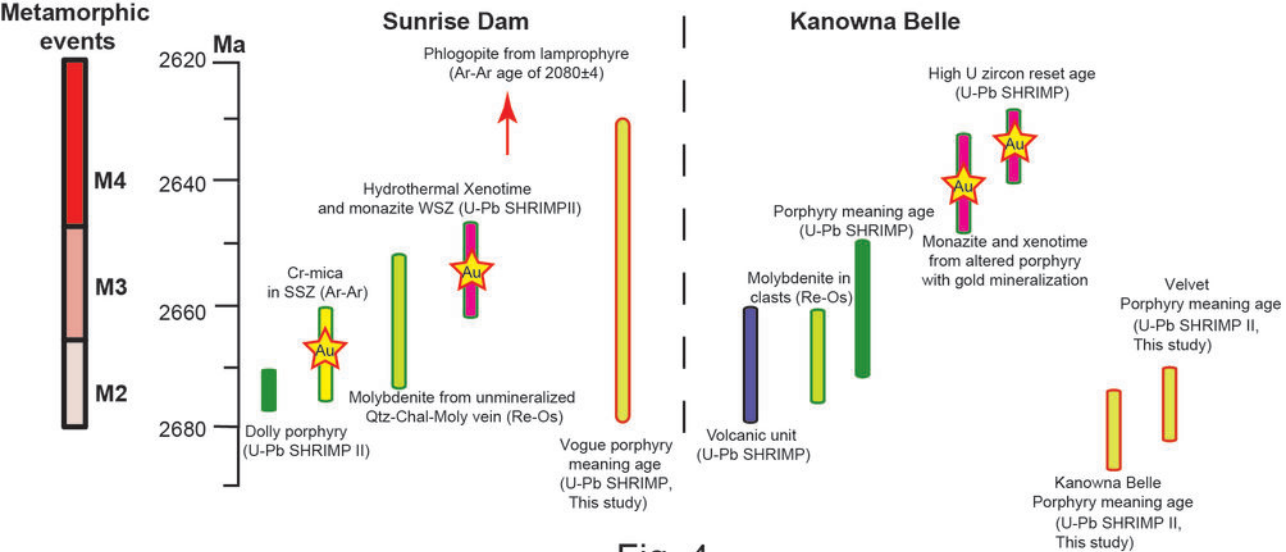
Metamorphic events
M4
M3
M2
Ma
2620
2640
2660
2680
Sunrise Dam
Phlogopite from lamprophyre
(Ar-Ar age of 2080±4)
Hydrothermal Xenotime
and monazite WSZ (U-Pb SHRIMPII)
Cr-mica
in SSZ (Ar-Ar)
Au
Molybdenite from unmineralized
Qtz-Chal-Moly vein (Re-Os)
Dolly porphyry
(U-Pb SHRIMP II)
Vogue porphyry
meaning age
(U-Pb SHRIMP,
This study)
Kanowna Belle
High U zircon reset age
(U-Pb SHRIMP)
Porphyry meaning age
(U-Pb SHRIMP)
Monazite and xenotime
from altered porphyry
with gold mineralization
Molybdenite in
clasts (Re-Os)
Volcanic unit
(U-Pb SHRIMP)
Velvet
Porphyry meaning age
(U-Pb SHRIMP II,
This study)
Kanowna Belle
Porphyry meaning age
(U-Pb SHRIMP II,
This study)

Fig. 4

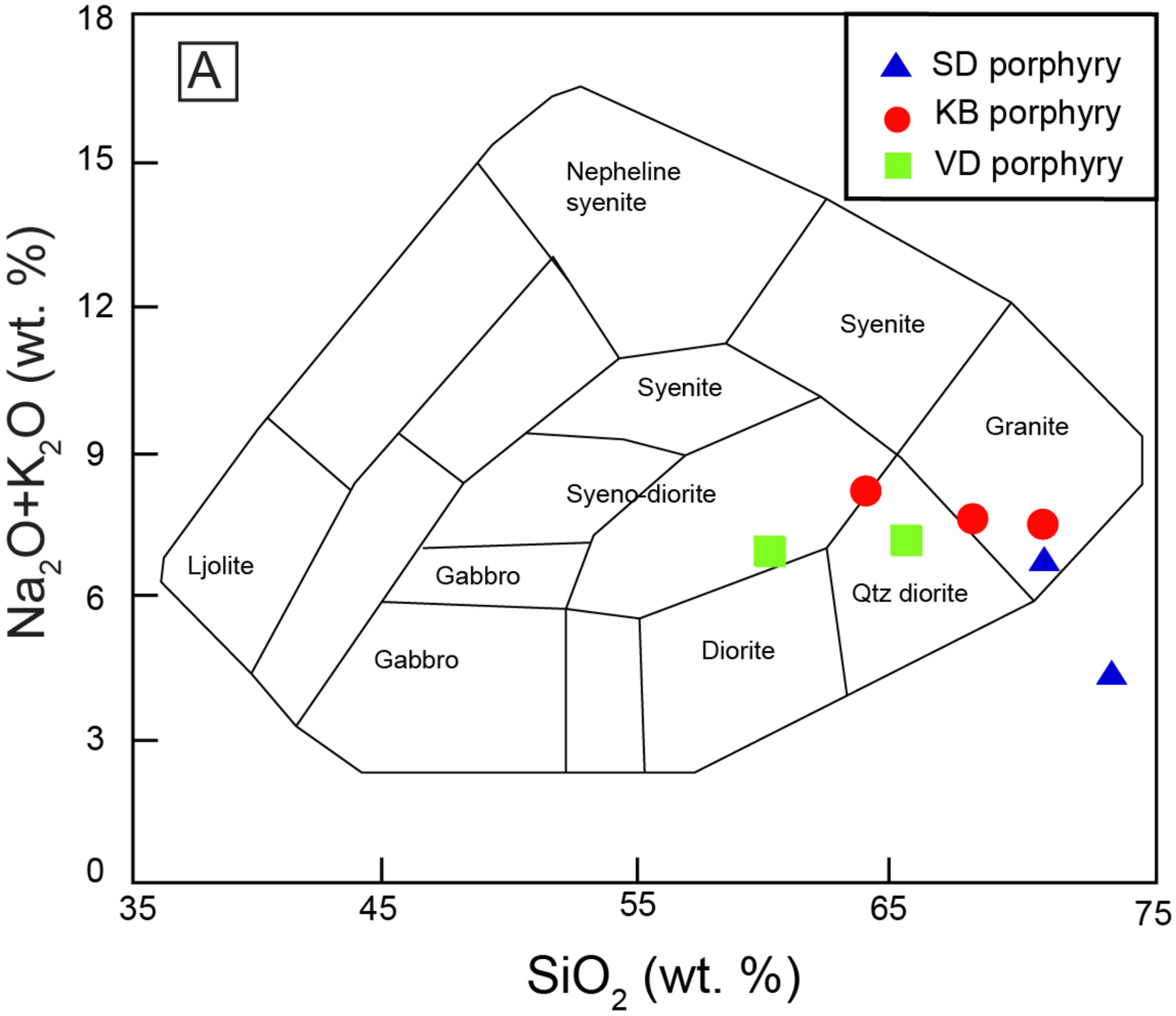
A
SD porphyry
KB porphyry
VD porphyry
Nepheline syenite
Syenite
Syenite
Granite
Syeno-diorite
Ljolite
Gabbro
Gabbro
Diorite
Qtz diorite
Na2O+K2O (wt. %)
SiO2 (wt. %)
0
3
6
9
12
15
18
35
45
55
65
75

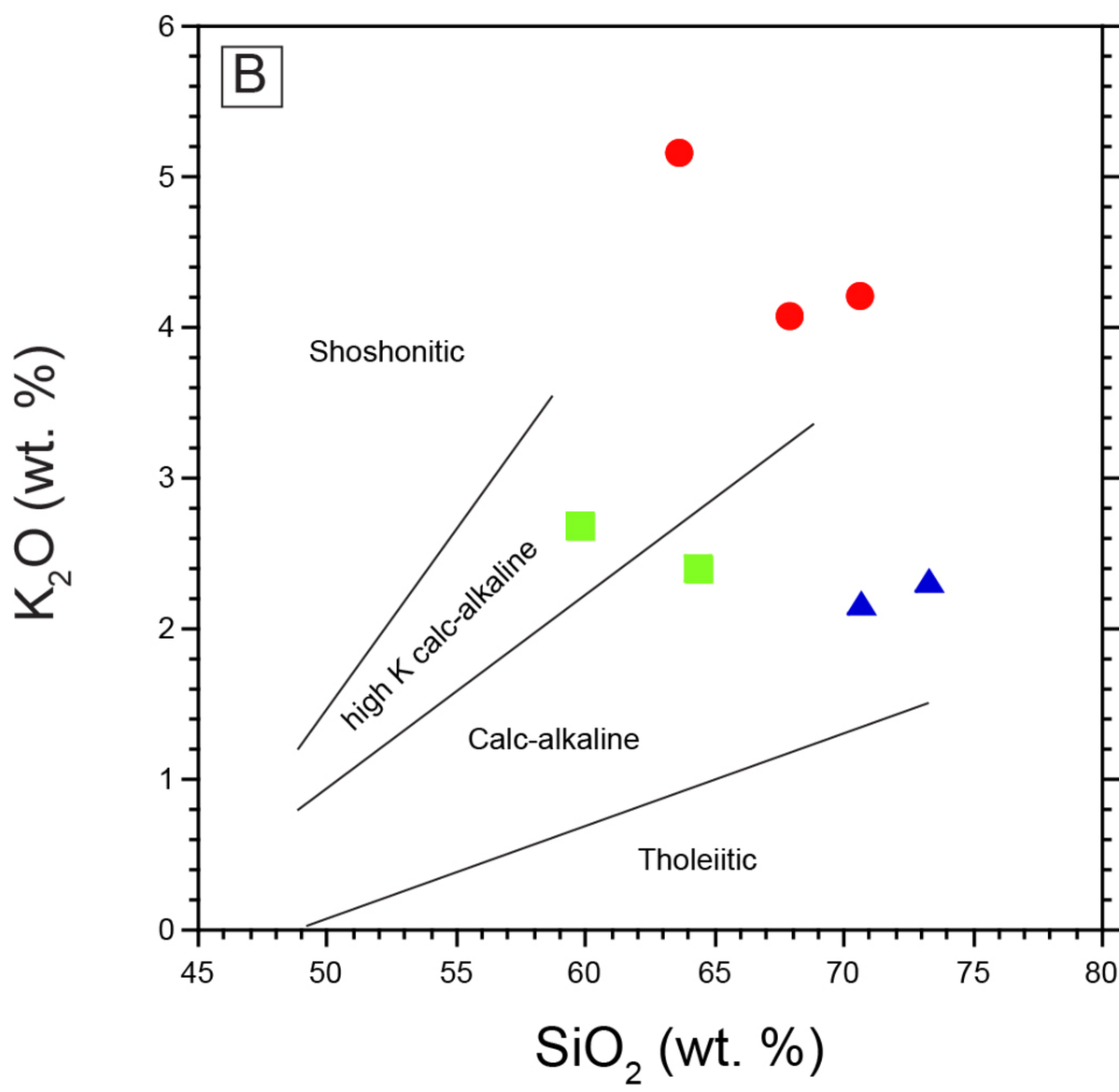
B
Shoshonitic
high K calc-alkaline
Calc-alkaline
Tholeiitic
K2O (wt. %)
SiO2 (wt. %)
0
1
2
3
4
5
6
45
50
55
60
65
70
75
80

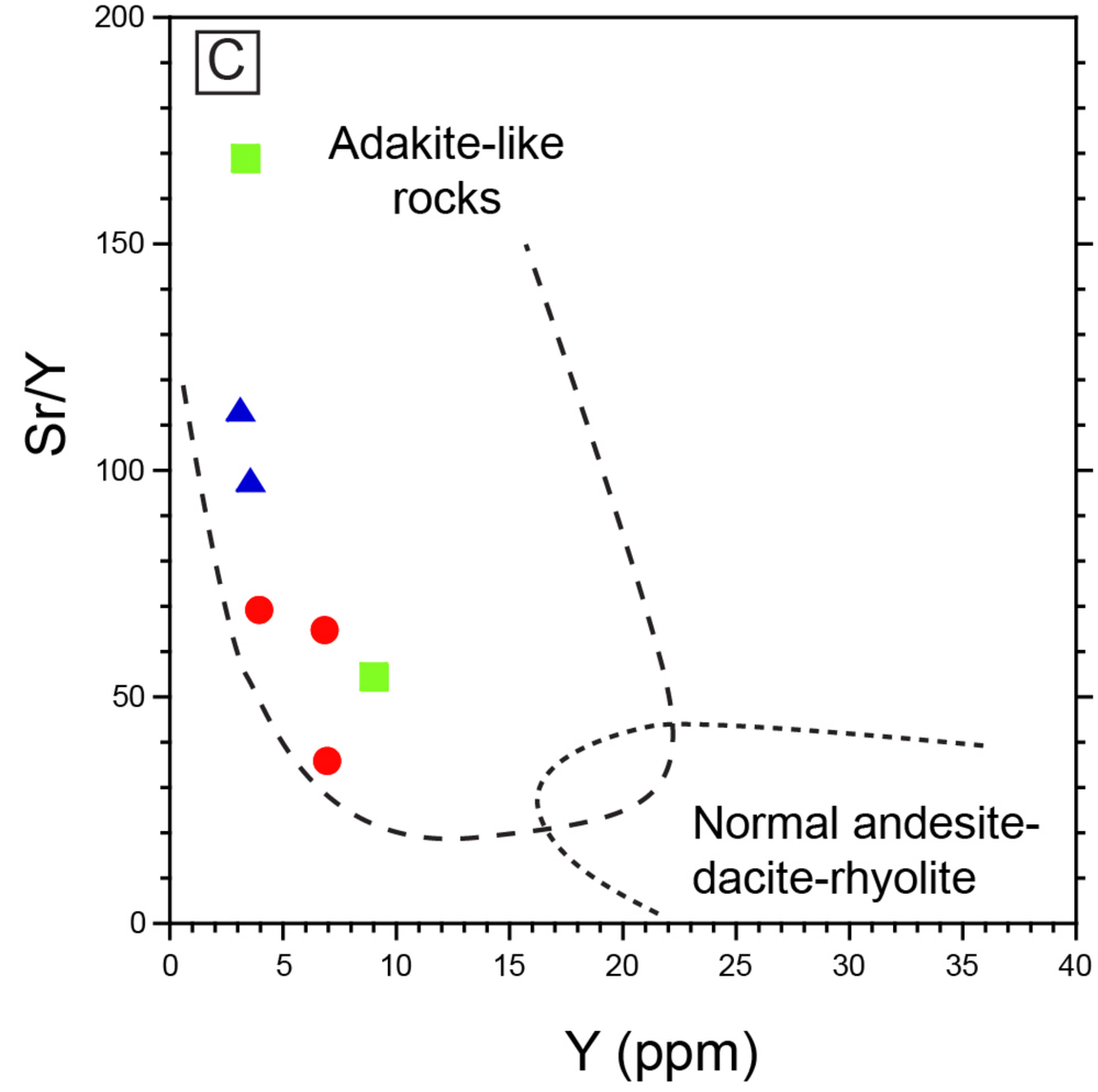
C
Adakite-like rocks
Normal andesite-dacite-rhyolite
Sr/Y
Y (ppm)
0
50
100
150
200
0
5
10
15
20
25
30
35
40

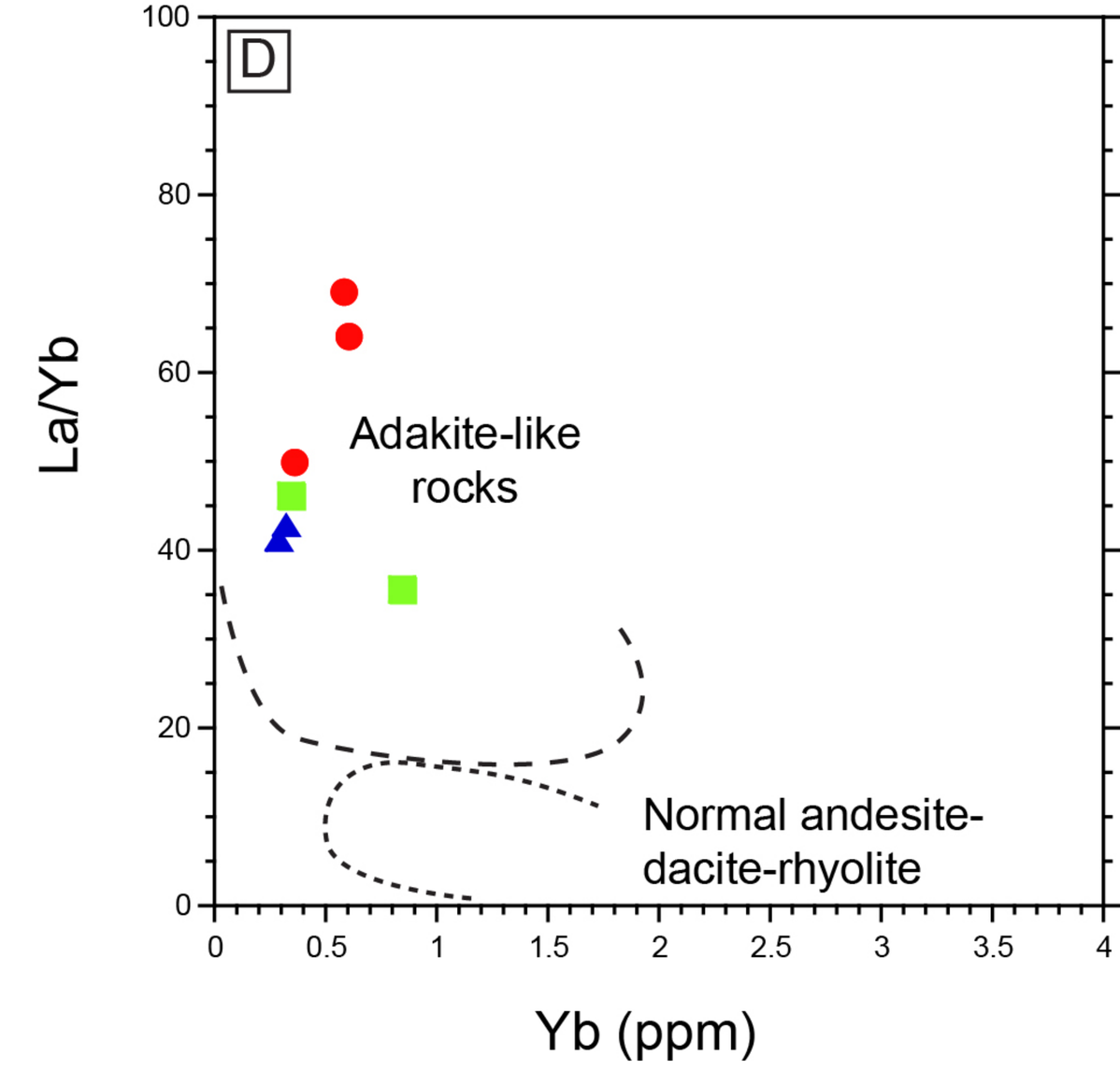
D
Adakite-like rocks
Normal andesite-dacite-rhyolite
La/Yb
Yb (ppm)
0
20
40
60
80
100
0
0.5
1
1.5
2
2.5
3
3.5
4

Fig. 5

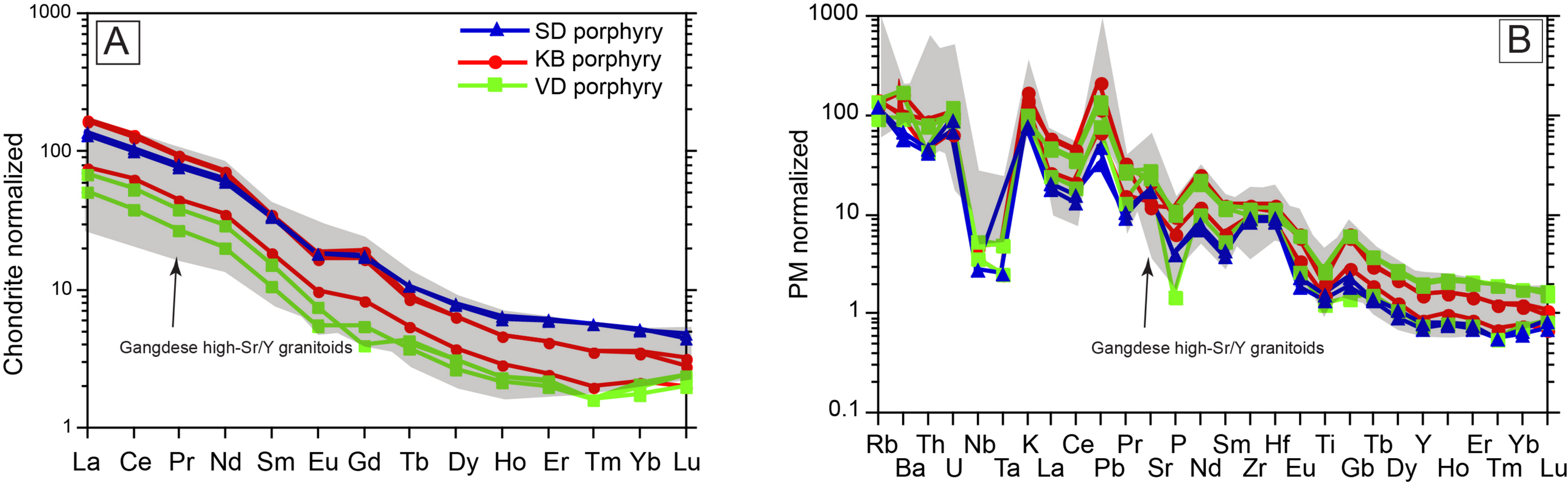
A
SD porphyry
KB porphyry
VD porphyry
Chondrite normalized
1000
100
10
1
Gangdese high-Sr/Y granitoids
La Ce Pr Nd Sm Eu Gd Tb Dy Ho Er Tm Yb Lu
B
PM normalized
1000
100
10
1
0.1
Gangdese high-Sr/Y granitoids
Rb Ba Th U Nb Ta K La Ce Pb Pr Sr P Nd Sm Zr Hf Eu Ti Gb Tb Dy Y Ho Er Tm Yb Lu

Fig. 6

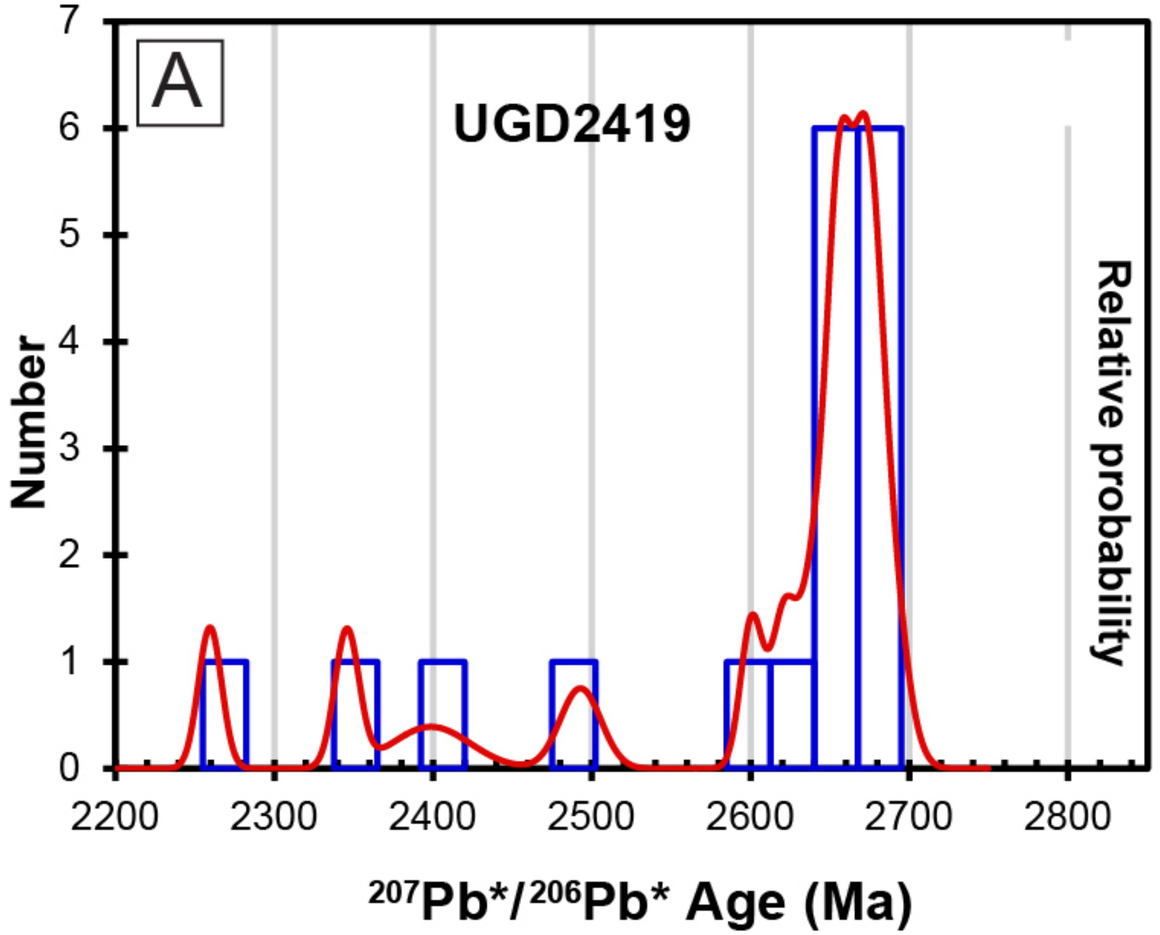
A
UGD2419
Number
Relative probability
0
1
2
3
4
5
6
7
2200
2300
2400
2500
2600
2700
2800
207Pb*/206Pb* Age (Ma)

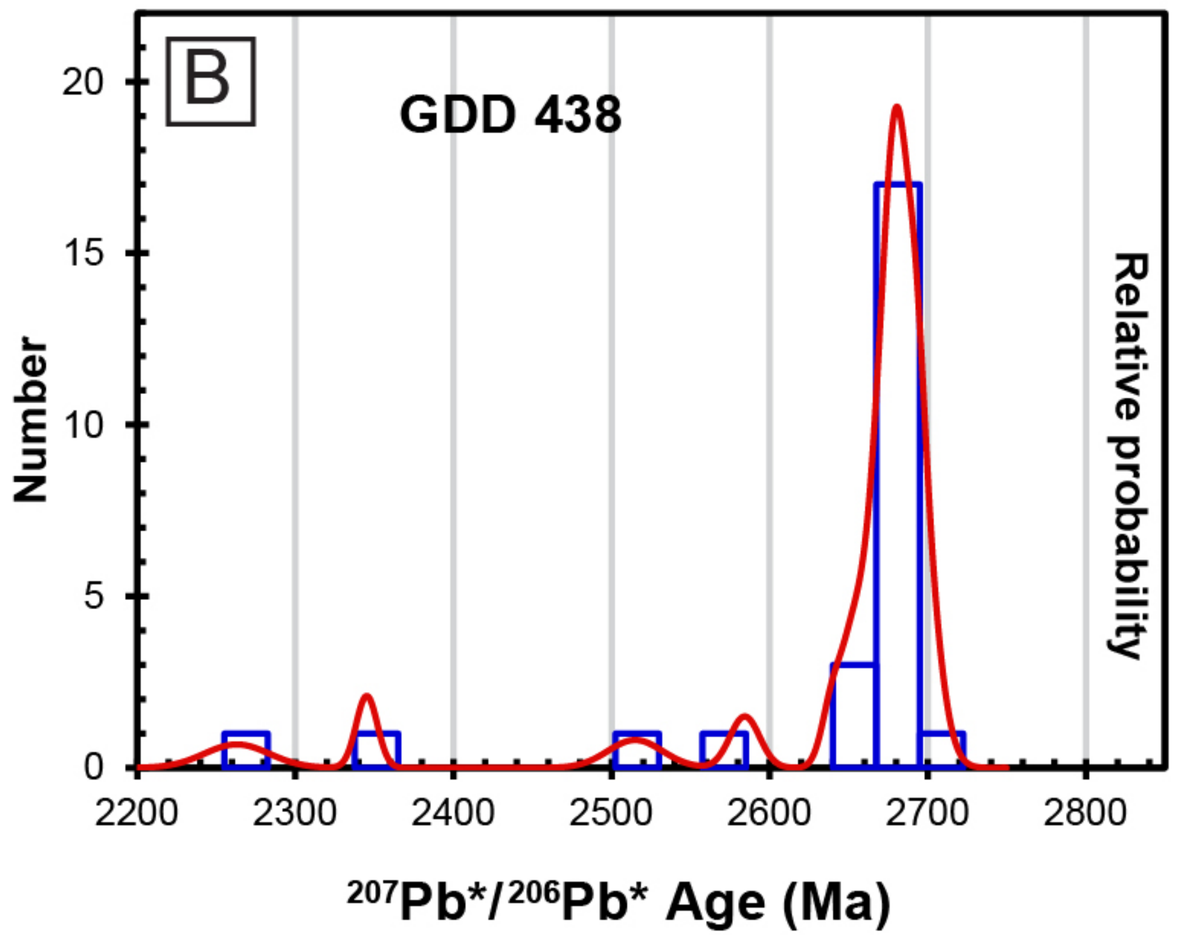
B
GDD 438
Number
Relative probability
0
5
10
15
20
2200
2300
2400
2500
2600
2700
2800
207Pb*/206Pb* Age (Ma)

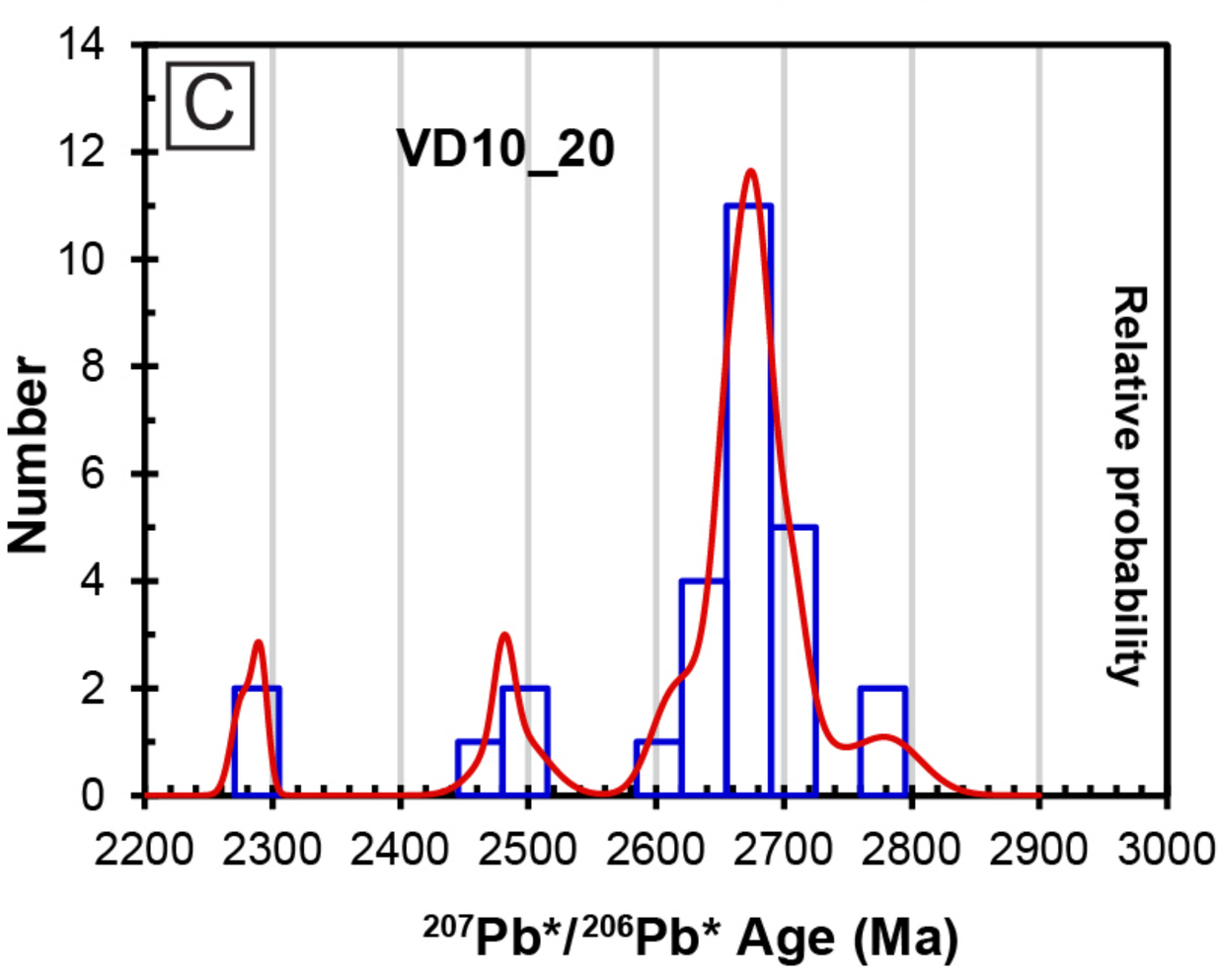
C
VD10_20
Number
Relative probability
0
2
4
6
8
10
12
14
2200
2300
2400
2500
2600
2700
2800
2900
3000
207Pb*/206Pb* Age (Ma)

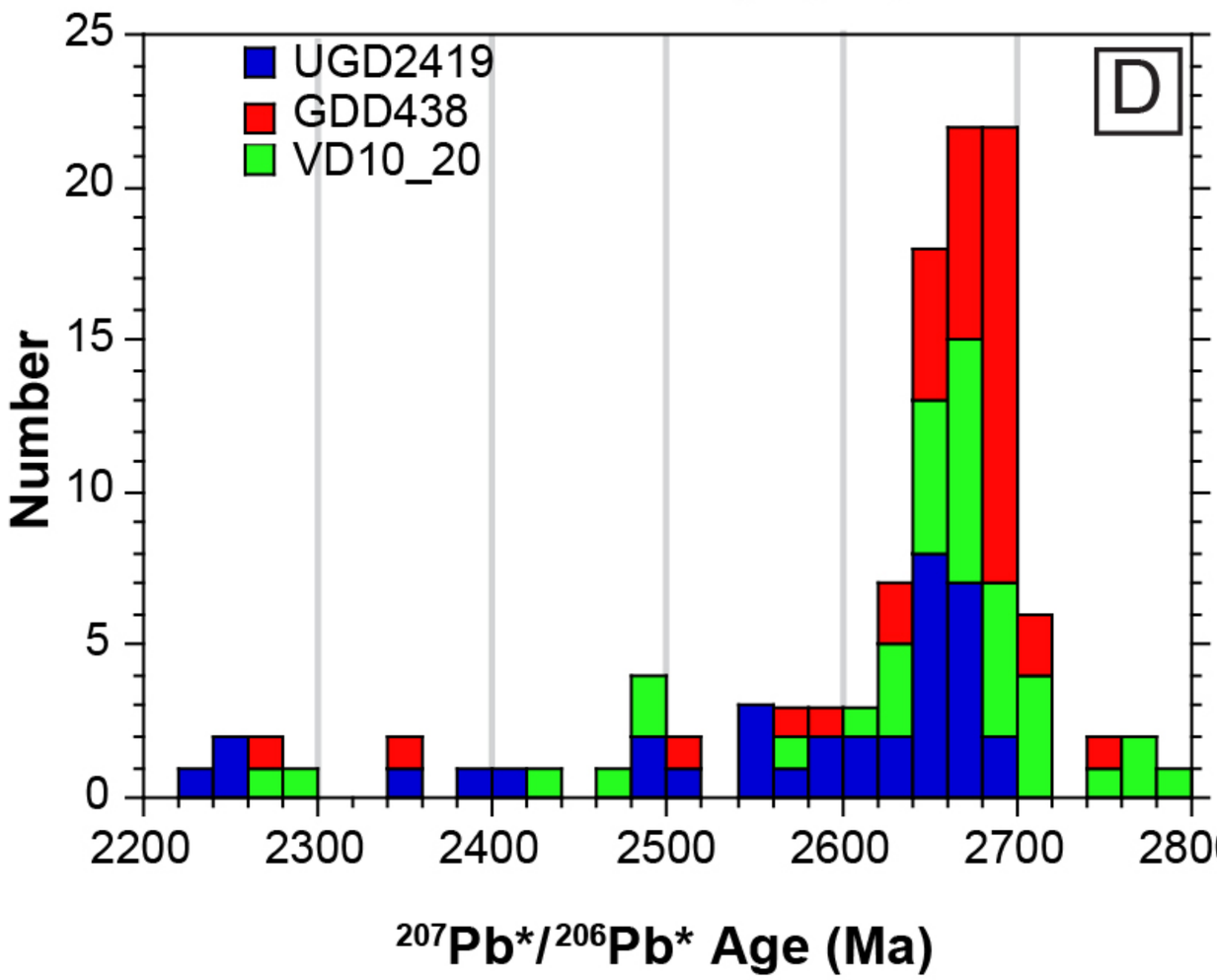
UGD2419
GDD438
VD10_20
D
Number
0
5
10
15
20
25
2200
2300
2400
2500
2600
2700
2800
207Pb*/206Pb* Age (Ma)

Fig. 7

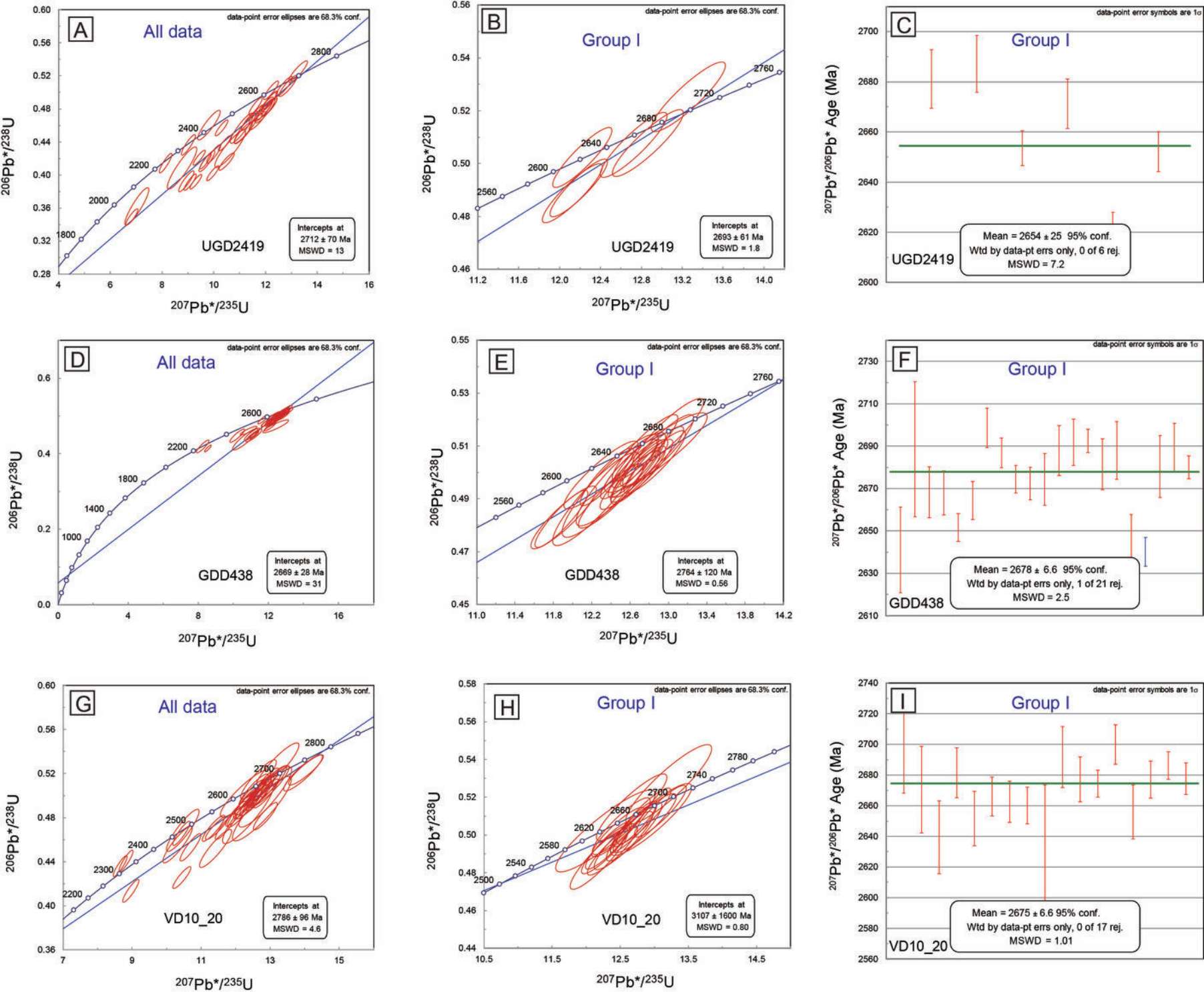
A
All data
data-point error ellipses are 68.3% conf.
Intercepts at
2712 ± 70 Ma
MSWD = 13
UGD2419
B
Group I
data-point error ellipses are 68.3% conf.
Intercepts at
2693 ± 61 Ma
MSWD = 1.8
UGD2419
C
Group I
data-point error symbols are 1σ
Mean = 2654 ± 25 95% conf.
Wtd by data-pt errs only, 0 of 6 rej.
MSWD = 7.2
UGD2419
D
All data
data-point error ellipses are 68.3% conf.
Intercepts at
2669 ± 28 Ma
MSWD = 31
GDD438
E
Group I
data-point error ellipses are 68.3% conf.
Intercepts at
2764 ± 120 Ma
MSWD = 0.56
GDD438
F
Group I
data-point error symbols are 1σ
Mean = 2678 ± 6.6 95% conf.
Wtd by data-pt errs only, 1 of 21 rej.
MSWD = 2.5
GDD438
G
All data
data-point error ellipses are 68.3% conf.
Intercepts at
2786 ± 96 Ma
MSWD = 4.6
VD10_20
H
Group I
data-point error ellipses are 68.3% conf.
Intercepts at
3107 ± 1600 Ma
MSWD = 0.80
VD10_20
I
Group I
data-point error symbols are 1σ
Mean = 2675 ± 6.6 95% conf.
Wtd by data-pt errs only, 0 of 17 rej.
MSWD = 1.01
VD10_20
206Pb*/238U
207Pb*/235U
207Pb*/206Pb* Age (Ma)

Fig. 8

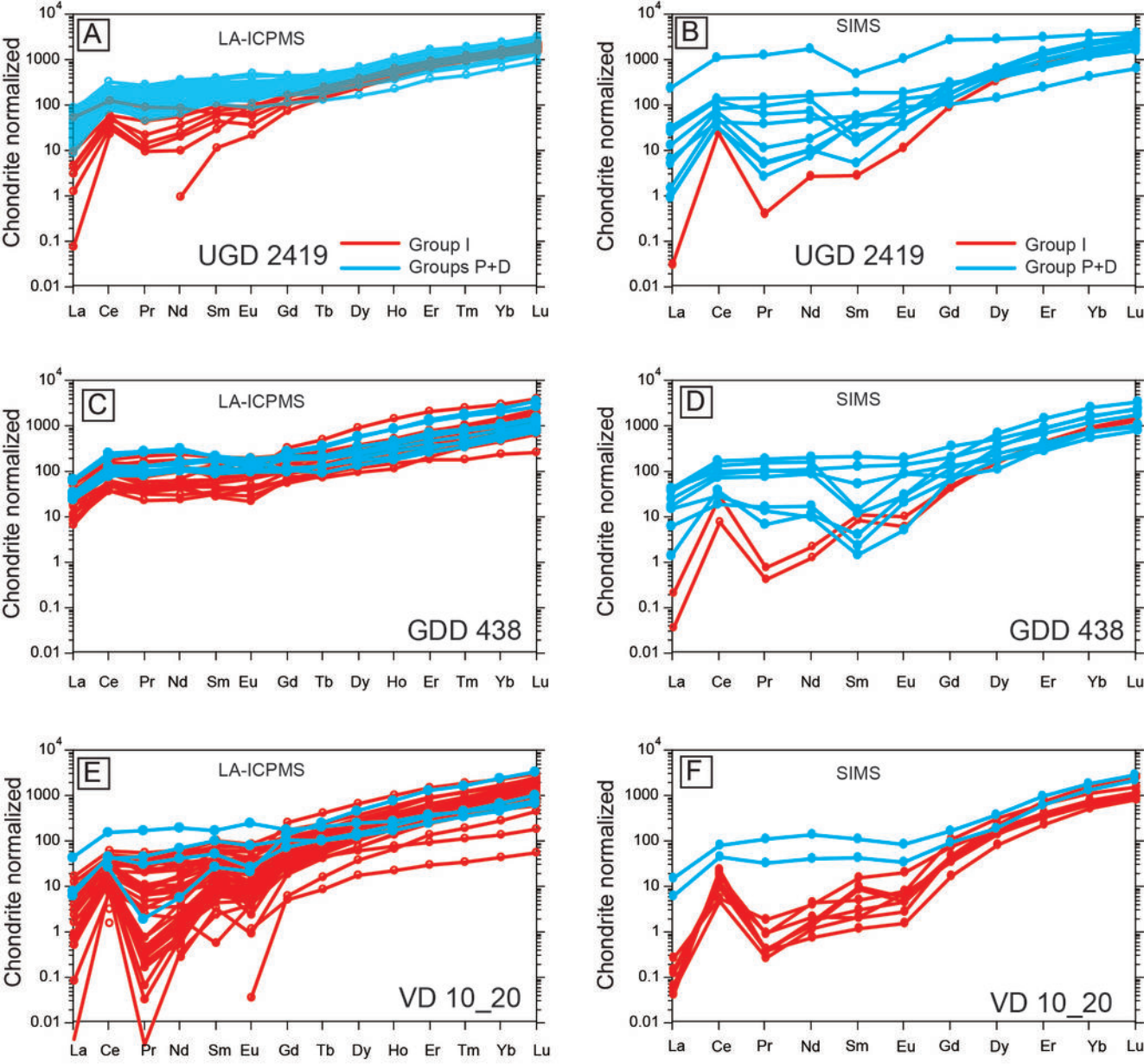
A
LA-ICPMS
UGD 2419
Group I
Groups P+D
B
SIMS
UGD 2419
Group I
Group P+D
C
LA-ICPMS
GDD 438
D
SIMS
GDD 438
E
LA-ICPMS
VD 10_20
F
SIMS
VD 10_20
Chondrite normalized
La Ce Pr Nd Sm Eu Gd Tb Dy Ho Er Tm Yb Lu

Fig. 9

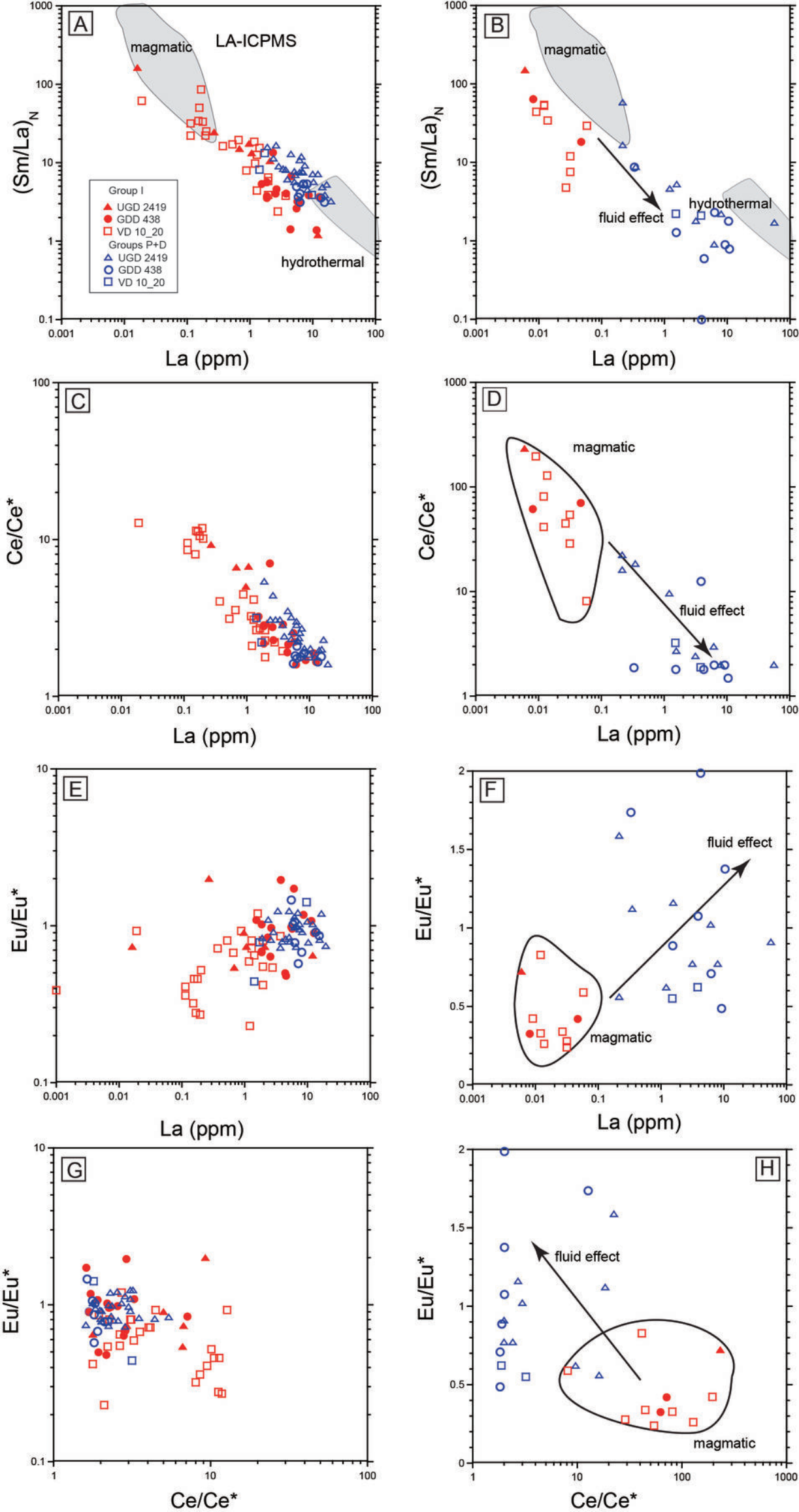
A
LA-ICPMS
magmatic
hydrothermal
Group I
UGD 2419
GDD 438
VD 10_20
Groups P+D
UGD 2419
GDD 438
VD 10_20
(Sm/La)N
La (ppm)
B
magmatic
fluid effect
hydrothermal
(Sm/La)N
La (ppm)
C
Ce/Ce*
La (ppm)
D
magmatic
fluid effect
Ce/Ce*
La (ppm)
E
Eu/Eu*
La (ppm)
F
fluid effect
magmatic
Eu/Eu*
La (ppm)
G
Eu/Eu*
Ce/Ce*
H
fluid effect
magmatic
Eu/Eu*
Ce/Ce*

Fig. 10

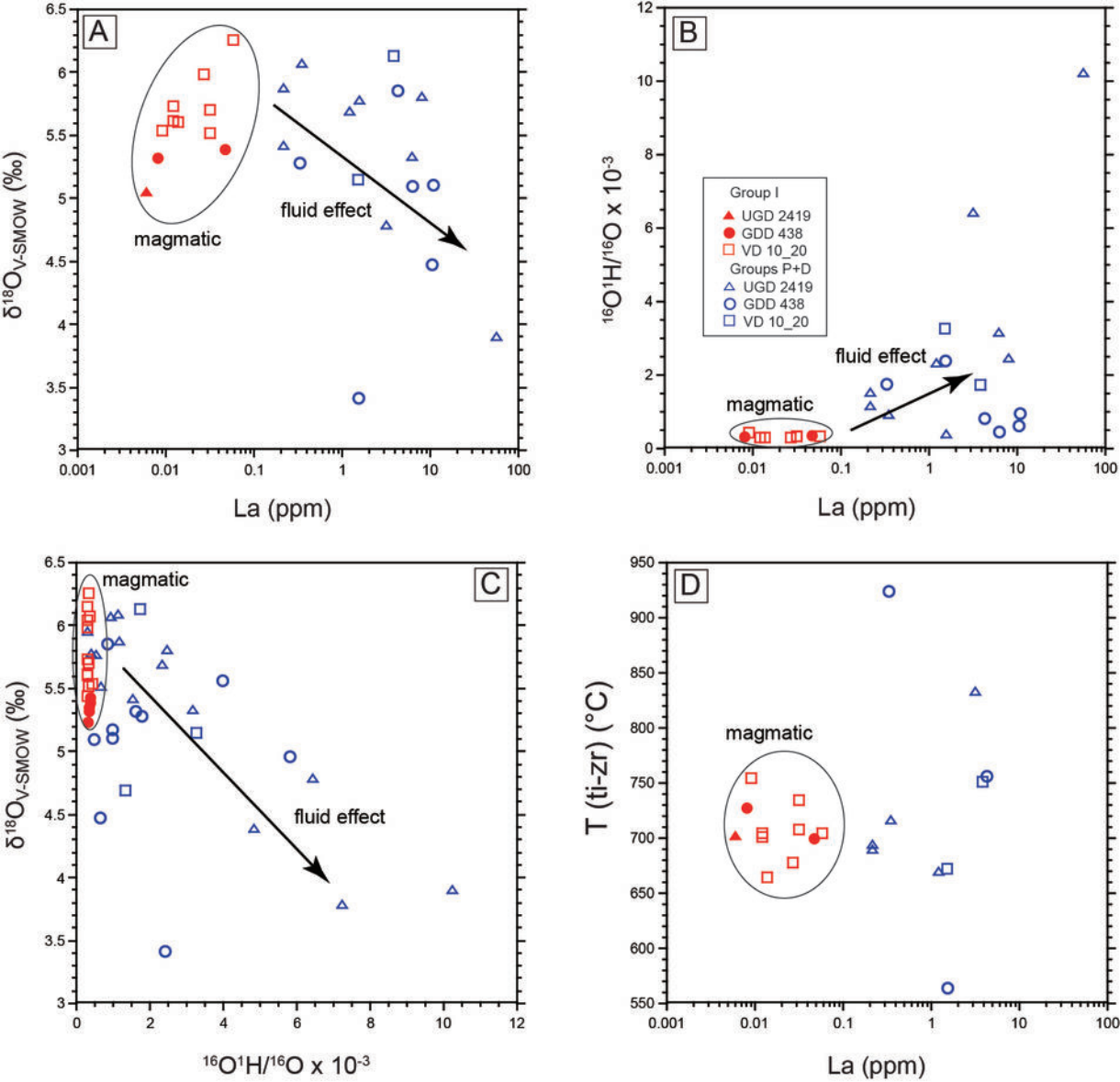
A
magmatic
fluid effect
δ18OV-SMOW (‰)
La (ppm)
B
Group I
UGD 2419
GDD 438
VD 10_20
Groups P+D
UGD 2419
GDD 438
VD 10_20
fluid effect
magmatic
16O1H/16O x 10-3
La (ppm)
C
magmatic
fluid effect
δ18OV-SMOW (‰)
16O1H/16O x 10-3
D
magmatic
T (ti-zr) (°C)
La (ppm)

Fig. 11

Table 1 Major and trace element compositions of granitoids from Sunrise Dam, Kanowna Belle, Velvet.

Number	2231-440.7 A	2419-45.5	GDD438-23 9	GDD438-32 0.8	GDD438-36 2.2	VD10_20-3 11	VD10_20-6 31
Location	Sunrise Dam	Sunrise Dam	Kanowna Belle	Kanowna Belle	Kanowna Belle	Velvet	Velvet
Lithology	granite	granite	granite	granite	syeno-diorite	granite	syeno-diorite
wt. %							
SiO_2	67.71	70.30	68.13	64.18	58.73	68.43	58.68
TiO_2	0.31	0.28	0.32	0.43	0.40	0.25	0.53
Al_2O_3	15.77	15.87	15.72	16.12	13.50	15.88	13.87
FeOT	1.95	2.51	2.66	2.80	2.42	1.59	4.68
MnO	0.03	0.03	0.03	0.04	0.05	0.02	0.07
MgO	1.00	1.22	1.12	1.40	3.85	0.88	2.48
CaO	2.75	1.96	1.45	2.37	5.88	1.74	4.37
Na_2O	4.11	1.44	2.94	3.16	2.64	3.98	4.10
K_2O	2.07	2.23	4.08	3.86	4.77	2.90	2.19
P_2O_5	0.08	0.08	0.13	0.23	0.19	0.03	0.21
Cr_2O_3	0.01	0.01	0.01	0.01	0.01	0.01	0.04
LOI	4.49	4.74	3.52	5.33	8.04	3.78	7.51
Total	100.28	100.67	100.11	99.93	100.48	99.49	98.73
ppm							
La	13.7	11.9	18	40.1	38.5	16.1	31.7
Ce	27	23.1	37.8	80.6	77.2	32.4	64
Pr	2.86	2.5	4.24	8.95	8.72	3.55	7.5
Nd	10.6	9.16	16.2	33.4	32.6	13.3	29.1
Sm	1.91	1.6	2.79	5.36	5.13	2.32	5.12
Eu	0.38	0.31	0.56	1.05	0.95	0.43	1.03
Gd	1.33	1.09	1.68	3.82	3.36	0.81	3.59
Tb	0.15	0.14	0.2	0.33	0.32	0.16	0.39
Dy	0.78	0.66	0.94	1.62	1.59	0.78	1.97
Ho	0.13	0.12	0.16	0.26	0.26	0.13	0.36
Er	0.36	0.32	0.4	0.68	0.69	0.35	0.99
Tm	0.04	0.04	0.05	0.09	0.09	0.04	0.14
Yb	0.32	0.29	0.36	0.58	0.6	0.35	0.87
Lu	0.06	0.05	0.05	0.07	0.08	0.06	0.11
Zr	91	100	102	139	124	101	128
Hf	2.5	2.8	2.7	3.7	3.2	2.8	3.4
U	1.42	1.81	1.32	2.14	1.98	2.54	1.96
Th	3.74	3.51	3.54	7.35	7.12	3.63	6.68
Sc	3	3	4	4	4	3	12
V	25	31	38	43	115	25	87

Co	4.1	12.8	8.3	11.1	9.1	4	30.4
Ni	13	17	38	22	22	16	196
Sb	19.1	23.6	22.8	10	25.3	10.6	28.9
Ba	464	383	670	696	1110	1200	804
Cs	8.5	11.5	6.2	7.4	4.8	10.9	12.1
Ga	16	17.1	17.7	19.8	15.6	20	18.2
Nb	1.9	1.9	2.5	3.5	3.3	2.5	3.7
Pb	5.8	8.7	12.3	39.8	21.1	14	25
Rb	76	75	87.9	84.4	78.2	85	57.5
Sr	352	352	274	250	442	568	492
Ta	< 0.1	0.1	0.1	0.2	0.2	0.1	0.2
Y	3.6	3.1	3.93	6.93	6.78	3.36	9.04
*Eu/Eu**	*0.73*	*0.72*	*0.79*	*0.71*	*0.70*	*0.96*	*0.73*
La/Yb	*42.81*	*41.03*	*50.00*	*69.14*	*64.17*	*46.00*	*36.44*
Sr/Y	*97.78*	*113.5*	*69.72*	*36.08*	*65.19*	*169.0*	*54.42*